Computational Neuroscience

ViSAPy: A Python tool for biophysics-based generation of virtual spiking activity for evaluation of spike-sorting algorithms

Espen Hagen [a,b,*], Torbjørn V. Ness [a], Amir Khosrowshahi [a,c,d], Christina Sørensen [e], Marianne Fyhn [e], Torkel Hafting [e], Felix Franke [f], Gaute T. Einevoll [a,g]

[a] Department of Mathematical Sciences and Technology, Norwegian University of Life Sciences, P.O. Box 5003, NO-1432 Aas, Norway
[b] Institute of Neuroscience and Medicine (INM-6) and Institute for Advanced Simulation (IAS-6), Jülich Research Centre and JARA, 52425 Jülich, Germany
[c] Redwood Center for Theoretical Neuroscience, University of California, Berkeley, CA 94720-3198, USA
[d] Nervana Systems, San Diego, CA 92121, USA
[e] Hafting-Fyhn Neuroplasticity Group, Department of Biosciences, University of Oslo, P.O. Box 1066 Blindern, NO-0316 Oslo, Norway
[f] Bio Engineering Laboratory, Department of Biosystems Science and Engineering, Swiss Federal Institute of Technology Zürich, CH-4058 Basel, Switzerland
[g] Department of Physics, University of Oslo, P.O. Box 1066 Blindern, NO-0316 Oslo, Norway

HIGHLIGHTS

- Efficient, accurate and validated automatic spike-sorting methods needed.
- Introduces `ViSAPy`, a Python tool for generating model-based benchmarking data sets.
- `ViSAPy` allows arbitrary electrode geometries, neuron models and realistic noise.
- Tetrode, polytrode (in vivo cortex) and MEA (in vitro retina) benchmark sets provided.

ARTICLE INFO

ABSTRACT

Background: New, silicon-based multielectrodes comprising hundreds or more electrode contacts offer the possibility to record spike trains from thousands of neurons simultaneously. This potential cannot be realized unless accurate, reliable automated methods for spike sorting are developed, in turn requiring benchmarking data sets with known ground-truth spike times.

New method: We here present a general simulation tool for computing benchmarking data for evaluation of spike-sorting algorithms entitled `ViSAPy (Virtual Spiking Activity in Python)`. The tool is based on a well-established biophysical forward-modeling scheme and is implemented as a Python package built on top of the neuronal simulator `NEURON` and the Python tool `LFPy`.

Results: `ViSAPy` allows for arbitrary combinations of multicompartmental neuron models and geometries of recording multielectrodes. Three example benchmarking data sets are generated, i.e., tetrode and polytrode data mimicking *in vivo* cortical recordings and microelectrode array (MEA) recordings of *in vitro* activity in salamander retinas. The synthesized example benchmarking data mimics salient features of typical experimental recordings, for example, spike waveforms depending on interspike interval.

Comparison with existing methods: `ViSAPy` goes beyond existing methods as it includes biologically realistic model noise, synaptic activation by recurrent spiking networks, finite-sized electrode contacts, and allows for inhomogeneous electrical conductivities. `ViSAPy` is optimized to allow for generation of long time series of benchmarking data, spanning minutes of biological time, by parallel execution on multi-core computers.

Conclusion: `ViSAPy` is an open-ended tool as it can be generalized to produce benchmarking data or arbitrary recording-electrode geometries and with various levels of complexity.

* Corresponding author at: Institute of Neuroscience and Medicine (INM-6) and Institute for Advanced Simulation (IAS-6), Jülich Research Centre and JARA, 52425 Jülich, Germany. Tel.: +49 2461 61 96668.
E-mail address: e.hagen@fz-juelich.de (E. Hagen).
URL: http://www.fz-juelich.de/inm/inm-6 (E. Hagen).

1. Introduction

Action potentials are the main carrier of information between neurons in the brain. They are characterized by fast inward and outward electrical currents across the cell membranes, resulting in transient deflections in the extracellular potential recorded in the vicinity of the source neurons. The extracellular waveforms of action potentials are commonly referred to as *spikes*. Spike waveforms recorded by extracellular recording devices vary in shape and amplitude between neurons due to morphological and electrical features of each neuron and position of the recording electrode (Henze et al., 2000; Gold et al., 2006, 2007, 2009; Pettersen and Einevoll, 2008). Extracellular recording devices typically record the combined activity of all nearby neurons, and it is not straightforward to assign individual spikes to individual neurons. However, in many applications it is crucial to know what neuron each spike came from, and this grouping process is referred to as *spike sorting* (Lewicki, 1998; Quiroga, 2007; Einevoll et al., 2012). An example illustration of such a spike-sorting process based on classification of waveforms is shown in Fig. 1. Here the final outcome is the assignment of recorded spikes to different neural sources illustrated with different colors. For a more detailed graphical overview of the steps involved in spike sorting, see Fig. 1 in Einevoll et al. (2012).

Spike sorting remains a formidable challenge in analysis of electrophysiological data: ideally, spike-sorting algorithms should be able to account for signals with poor signal-to-noise ratios, temporally overlapping spikes from several neurons, waveforms with a wide variety of spatiotemporal shapes (i.e., temporal shapes recorded simultaneously on several electrode contacts), waveforms that depend on the on-going neuronal firing dynamics (e.g., bursting/non-bursting, adaptation), and waveforms that change over the time-course of the measurement (Franke et al., 2010; Einevoll et al., 2012). Traditional spike-sorting procedures for recordings with one or just a few electrode channels involve a major manual component, and are therefore both idiosyncratic and labor intensive (Harris et al., 2000; Wood et al., 2004; Einevoll et al., 2012). The new generation of silicon-based multielectrodes with hundreds or more electrode contacts (Buzsáki, 2004; Blanche et al., 2005; Frey et al., 2009; Lambacher et al., 2011; Fiscella et al., 2012; Einevoll et al., 2012) offers exciting opportunities for simultaneous spike-train recordings from thousands of neurons. However, this potential can only be realized if these advances in electrode
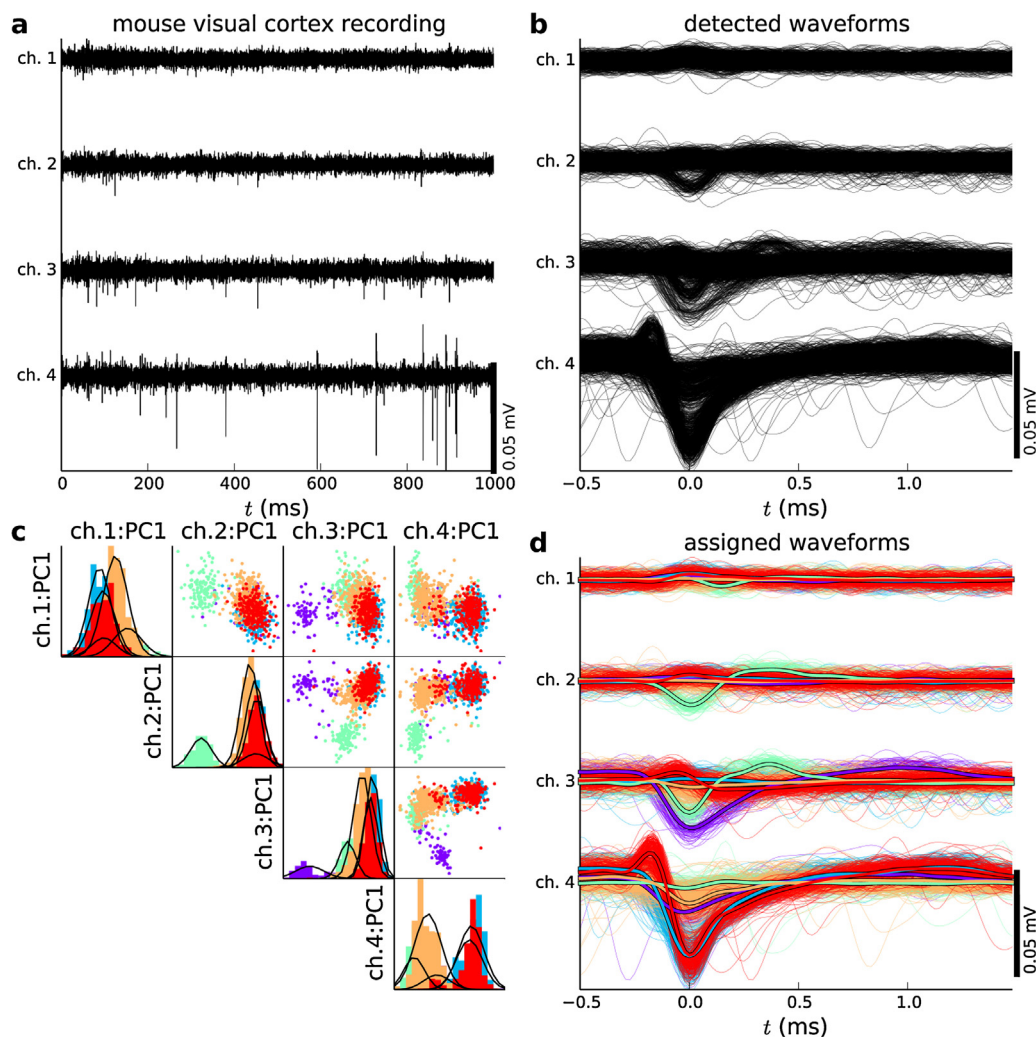
Fig. 1. Spike-sorting problem exemplified by offline spike sorting of *in vivo* tetrode data measured in mouse visual cortex. (a) Band-pass filtered recordings expose spiking events (for filter settings see Section 2.7). (b) Spike waveforms across electrode channels extracted from band-pass filtered data, aligned to their minima. (c) Clustered projections of principal component 1 (PC1) of detected waveforms with corresponding distributions in each electrode channel. (d) Clustered waveforms across electrode channels. Detection, clustering and sorting were performed using the SpikeSort package in Python (http://spikesort.org). Spikes were detected on ch. 3 and ch. 4, with a down-slope threshold of 10 μV, ± 1 ms alignment window, and removal of duplicates within ± 0.25 ms. Features were clustered using the K-means++ algorithm (Arthur and Vassilvitskii, 2007) on the first two principal components of the waveforms across each electrode channel, assuming five spiking neurons to be present in the recording.
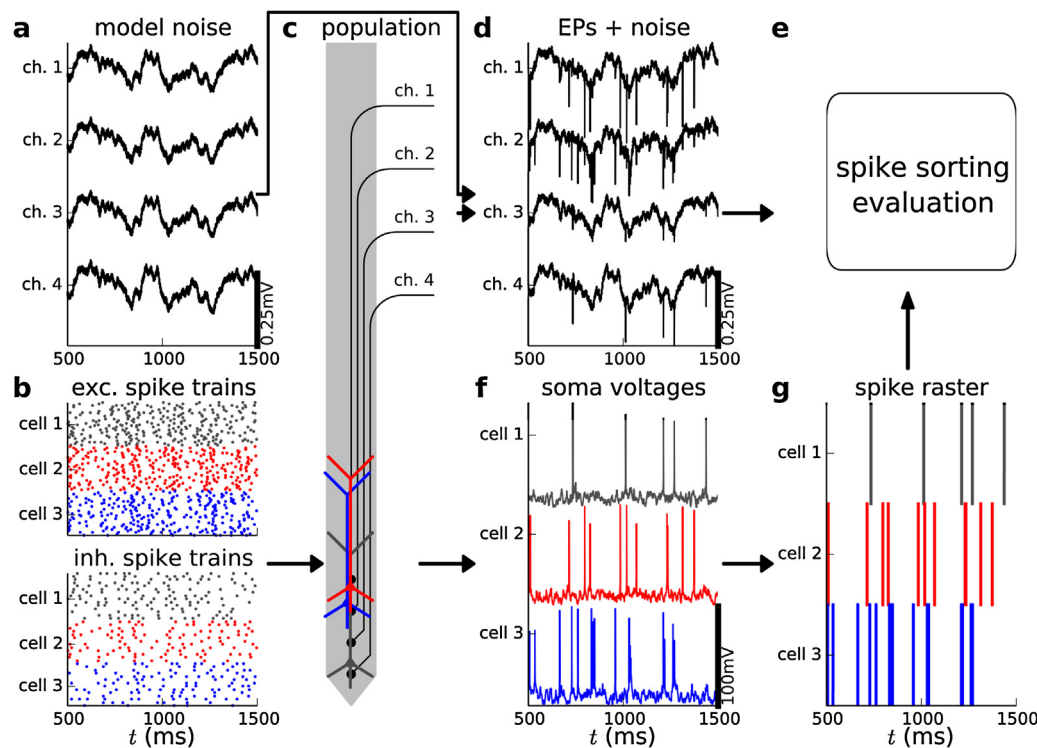
Fig. 2. Schematic illustration of framework for generation of model benchmarking data where ground truth is known, mimicking an *in vivo* situation. (a) Extracellular noise generated from a descriptive noise model mimicking experimental noise, Section 2.6. (b) Raster plots of excitatory and inhibitory synapse activation times for conductance-based excitatory and inhibitory synapses, Section 2.3. Each row of dots represent synaptic activation times from presynaptic neurons, and the colors signify the postsynaptic target cell. (c) Recording device (here a linear tetrode) with population of biophysically detailed multicompartment model neurons, Section 2.2. (d) Superposition of extracellular potentials (EP) from model population and synthetic noise. (f) Somatic membrane potential from each spiking model neuron used to assess the ground-truth spike times (g) which allows for unambiguous evaluation (e) of the result from applying spike-sorting algorithms on extracellular model data (d). (For interpretation of the references to color in this figure legend, the reader is referred to the web version of the article.)

hardware are accompanied by the development of accurate and reliable automatic methods for spike-train extraction (Lewicki, 1998; Quiroga, 2007; Einevoll et al., 2012; Franke et al., 2012).

Methods for reduction of manual involvement in spike sorting have been, and still are, an active topic of research (Lewicki, 1998; Quiroga, 2007; Einevoll et al., 2012), but the problem remains largely unresolved. Numerous automatic spike-sorting algorithms have been developed, but their accuracy have been difficult to assess due to lack of suitable benchmarking data sets for systematic evaluation of their performance. While measures on the performance of spike-sorting algorithms without explicit knowledge about the underlying activity can be constructed (Hill et al., 2011), comprehensive evaluation of such algorithms require access to benchmarking spike-data sets where the *ground truth*, i.e., the underlying neuronal spike trains, are known (Einevoll et al., 2012). Such ground-truth data sets, analogous to well-established benchmarking data sets in computer science (Hockney, 1996), can in principle be obtained experimentally by means of joint intracellular and extracellular recordings of action potentials (Henze et al., 2000; Harris et al., 2000), but such double recordings are difficult to do, and in practice limited to a modest number of neurons.

A natural alternative is to use synthetic benchmark data, either constructed from experimentally measured spike waveforms (Wood et al., 2004; Thorbergsson et al., 2010), biophysical forward modeling (Menne et al., 2002; Eaton and Henriquez, 2005; Smith and Mtetwa, 2007; Franke et al., 2010; Thorbergsson et al., 2002), or a combination of both (Martinez et al., 2009; Camuñas Mesa and Quiroga, 2013). A limitation with use of experimentally recorded waveform templates is that not only the spike amplitude, but also the spike shape, depend on electrode position. Thus the

generated benchmark data will *a priori* be limited to testing spike-sorting algorithms in situations very similar to those for which the templates were recorded (e.g., similar electrode types, similar neuron morphologies and dynamics, similar brain states, and similar distances between neuron and electrode contacts). A further complication is that even with fixed electrode positions, the spike waveform may be non-stationary, i.e., vary with time. For example, during bursting behavior where a handful of spikes are fired in rapid succession, the amplitude of the successive spikes is generally seen to decrease (Ranck, 1973; Fee et al., 1996; Quirk and Wilson, 1999; Harris et al., 2001; Delescluse and Pouzat, 2006; Stratton et al., 2012).

Generation of benchmarking data by means of biophysical forward modeling has no such principled limitations. This approach takes advantage of the well-known biophysical cable properties of neurons, and the link between intracellular and extracellular potentials provided by volume conduction theory (Rall, 1962; Holt and Koch, 1999). The theory allows for detailed simulation of the extracellular signatures of spikes and how they depend on, e.g., position of the electrode relative to the neuron, neuronal morphology and dynamic state, as well as the surrounding network and level of firing synchrony (Gold et al., 2006, 2007; Pettersen et al., 2008; Pettersen and Einevoll, 2008; Franke et al., 2010; Thorbergsson et al., 2002; Camuñas Mesa and Quiroga, 2013). Such forward modeling typically proceeds in two steps (Lindén et al., 2014). First, the transmembrane neuronal currents during action-potential firing are calculated using multicompartmental modeling. Next, the extracellular potential is found by summing over the transmembrane current of each compartment, inversely weighted with the distance between the neuronal compartment and the (virtual) electrode contact points.

We here present ViSAPy (Virtual Spiking Activity in Python), a general simulation tool based on this biophysical forward-modeling scheme, for generation of benchmark data for evaluation of spike-sorting algorithms. ViSAPy has a modular design, and the illustration in Fig. 2 presents the main steps in benchmark data generation. For a benchmark dataset emulating an *in vivo* tetrode recording, we first generate synthetic noise signals with frequency content and covariance between channels extracted from experimental recordings (Fig. 2a). We then generate activation times for excitatory and inhibitory synaptic events (Fig. 2b) that in turn are spatially distributed across the morphologies of several biophysically detailed, multicompartmental model neurons positioned in close proximity of the electrode contacts (Fig. 2c). From the multicompartment neuron models we compute the extracellular potential across electrode contacts, i.e., recording channels, and subsequently superimpose the synthetic noise (Fig. 2d). The resulting traces represent benchmarking data to be used as input when testing different spike-sorting algorithms (including preprocessing steps). From the somatic membrane voltages in each neuron (Fig. 2f) we extract the ground-truth spiking activity (Fig. 2g), hence allowing for a direct comparison between estimated spike trains and the ground truth during the evaluation step (Fig. 2e). In ViSAPy each main component of the model setup illustrated in Fig. 2a–c is represented as programming objects, hence the individual components such as neuron models, synaptic stimulation models and electrode models may be exchanged or modified at wish depending on the application.

The ViSAPy tool is implemented as a Python[1] package (Langtangen, 2009) building on top of the neuronal simulator NEURON (Hines et al., 2009) and the Python tool LFPy for calculating extracellular potentials (Lindén et al., 2014). ViSAPy relies on NEST (Gewaltig and Diesmann, 2007) for simulations of point-neuron network simulations providing synaptic input onto the multicompartmental neurons generating the extracellular potential. ViSAPy allows for (i) use of arbitrary combinations of multicompartmental neuron models, (ii) arbitrary geometries of recording electrodes (e.g., single electrodes, tetrodes (Gray et al., 1995), polytrodes, i.e., linear multielectrodes (Ulbert et al., 2001; Blanche et al., 2005), microelectrode arrays (MEAs) (Taketani and Baudry, 2006)), (iii) finite-sized electrode contacts, (iv) addition of realistic background noise extracted directly from experiments, and (v) tailored excitatory and inhibitory synaptic activation to, e.g., drive the spiking neurons with well-controlled correlated synaptic inputs. Importantly, ViSAPy has been optimized to allow for generation of long time series of benchmark data, spanning minutes of biological time, by parallel execution on multi-core computers. ViSAPy is made available on GitHub (http://github.com/espenhgn/ViSAPy), is open source and released under GPLv3.[2]

To illustrate the application of ViSAPy, three different electrode configurations are considered: a tetrode with four closely spaced electrode contacts, a polytrode, i.e., (linear) multielectrode, with 16 contacts positioned along a line, and a two-dimensional electrode contact grid (microelectrode array, MEA) comprising 102 electrode contacts. Tetrodes and polytrodes are typically used in *in vivo* recordings in cortex or hippocampus, and in the present examples we generated virtual spike data for these recording devices from a set of biophysically detailed layer-5b pyramidal model cells (Hay et al., 2011) with background noise extracted from *in vivo* experiments superimposed on the signal. Interestingly, we found that with our *in vivo*-like synaptic inputs (generated by separate simulations of leaky integrate-and-fire (LIF) neurons in recurrent networks), a biologically plausible spike waveform variability was automatically

obtained in the simulations. In the MEA example, where the heterogenous electrical conductivity from the electrode device, tissue and saline influence the spike waveforms compared to the typical *in vivo* situation (Ness et al., 2012, 2015), we made benchmarking data mimicking *in vitro* recordings of spiking retinal ganglion cells (Segev et al., 2004).

While our focus is on generating benchmarking data for testing of spike-sorting algorithms, ViSAPy can also give direct insight into the link between neural activity and what is measured with extracellular electrodes (Holt and Koch, 1999; Gold et al., 2006; Pettersen et al., 2008, 2012; Pettersen and Einevoll, 2008; Lindén et al., 2010, 2011; Einevoll et al., 2013a,b; Łęski et al., 2013; Reimann et al., 2013). Note also that the biophysical forward-modeling scheme in ViSAPy is not only applicable for modeling spikes. The tool is equally suitable for calculating the low-frequency components of the extracellular potential, i.e., the local field potential (Einevoll et al., 2013a,b).

The paper is organized as follows: The methods behind ViSAPy are presented in Section 2. In Section 3 we first consider in detail the properties of the extracellular spike from the layer-5b cortical model cell (Hay et al., 2011), investigating how the spike waveform depends on electrode size and neuronal state (in particular how the spike waveform depends on the time since the previous spike). Finally, we show example results for generated benchmarking data for the tetrode, polytrode and MEA, respectively.

2. Materials and methods

2.1. Experimental procedures

In order to produce both example data (cf. Fig. 1) and realistic models for background noise to use in the generation of benchmarking data, experimental recordings were made in visual cortex of a CB57 mouse (3 months old). The animal was sedated with an intramuscular injection of chlorprothixene (0.2 mg in 0.05 ml sterile water), and anesthetized with 1–2% isoflurane in air (80 ml min^{-1}). To achieve mydriasis and cycloplegia, tropicamide was applied to the eyes (one drop per eye). Silicone oil was applied to prevent drying and cataract, yet allowing clear optical transmission. The animal was maintained at 37 °C (MouseStat system). The scalp was retracted and a craniotomy performed (2 mm in diameter, 1 mm anterior and 3 mm lateral to lambda). The exposed cortical surface was covered with artificial cerebrospinal fluid (Harvard Apparatus). The electrode was lowered into the brain to a depth of 1000 μm in the center of the craniotomy, and was allowed to settle for 20 min before recording. Recordings were made with a polytrode (linear multicontact silicone probe) from NeuroNexus with 16 sites spaced at 50 μm intervals (A1×16-3mm-50-177-A16). The polytrode was connected to the recording equipment (Axona, Herts, U.K.) via AC-coupled unity-gain operational amplifiers close to the animal's head. Continuous sampling of unfiltered raw data at 16 bit and 48 kHz was done for a duration of 10 min. Drifting gratings (Psychophysics Toolbox (Brainard, 1997) w. MATLAB (The Mathworks, Inc)) were displayed on a 21 in. monitor placed 25 cm in front of the animal. The experiments were performed in accordance with the Norwegian Animal Welfare Act and the European Convention for the Protection of Vertebrate Animals used for Experimental and Other Scientific Purposes.

Recordings were converted to floats in units of mV and post-processed offline in Python. For spike detection and to reduce spurious signals common to all electrode channels, the spatial mean raw potentials, i.e., mean potential across all channels, at each time step was subtracted from each electrode channel, prior to band-pass filtering (cf. Section 2.7). After filtering, peaks in the power spectrum caused by noise, i.e., 50 Hz line noise, 62 Hz screen refresh

rate and associated harmonics, were attenuated by more than five orders of magnitude. Some auxiliary steps to reduce noise in the raw recordings used for generation of synthesized noise (cf. Section 2.6) were taken, as mean subtraction as above did not give the desired effect: An additional series of narrow, causal notch filters were applied to the raw recordings reducing spurious frequency peaks present in the power spectral density (PSD) that we identified by visual inspection. Band-stop Butterworth filters were designed with `scipy.signal.iirdesign` (1.5 dB minimum attenuation in stop-band, 0.5 dB maximum loss in pass-band, each centered at $f = [50, 62, 88, 100, 112, 150, 250, 1910]$ Hz, stop-band was $f \pm 1$ Hz, pass-band $f \pm 5$ Hz). A butterworth aliasing filter with 1 dB maximum loss in pass-band at 13 kHz, 9 dB minimum attenuation in stop-band at 14 kHz was applied.

2.2. Multielectrode models

ViSAPy allows for single electrodes and multielectrodes with arbitrary electrode numbers and three-dimensional layouts. Here, we considered three commonly used multielectrode configurations as examples.

Tetrode. We emulated the layout of a NeuroNexus tetrode device (type Q1×1-10mm-50-177). The $n_{contacts} = 4$ electrode contacts were positioned 50 μm apart along the vertical z-axis. We further assumed circular electrode contacts with radius $r_{contact} = 7.5$ μm (177 μm^2 surface area). The electrode shaft (probe) had a rectangular cross-section, i.e., 50 μm thick and 80 μm wide with the front-face of the shaft (where the contacts are placed) being centered along the z-axis. The shaft width was tapered to a tip starting at the depth of the lowest electrode and ending 50 μm below, illustrated in Fig. 2c.

Polytrode. We also emulated a polytrode geometry similar to the electrode used to record our experimental data. This NeuroNexus device (A1×16-3mm-50-177-A16) has $n_{contacts} = 16$. As for the tetrode, the electrode contacts were aligned along the vertical axis with an inter-contact distance of 50 μm. Electrode contacts and shaft profile were otherwise as for the tetrode.

Microelectrode array (MEA). For benchmarking data emulating *in vitro* recordings, we focused on the Hierlemann high-density microelectrode array (Frey et al., 2009, 2010; Hierlemann et al., 2011; Fiscella et al., 2012). This MEA has 11,011 electrodes arranged in a honeycomb pattern, from which up to 126 can be freely chosen and recorded from simultaneously. Each contact point diameter is 7 μm, and the inter-contact distance is 18 μm (Frey et al., 2009, 2010). We emulated this close-packed electrode arrangement with 6 columns and 17 rows totaling 102 electrode contacts.

2.3. In vivo cortical data for tetrodes and polytrodes

Neuron models. For benchmarking data mimicking *in vivo* tetrode and polyelectrode recordings in cortex, we used biophysically detailed, multicompartment models of L5b pyramidal neurons from rat neocortex taken from a study by Hay et al. (2011). In Hay et al. (2011) these models were fitted using an evolutionary multi-objective optimization algorithm to reproduce intracellular responses obtained in whole-cell multi-patch recordings (Deb and Kalyanmoy, 2001; Druckmann et al., 2007; Van Geit et al., 2008; Hay et al., 2011, 2013; Bahl et al., 2012). The model files were downloaded from ModelDB[3] (Hines et al., 2004). We selected these models due to their ability of showing complex firing behavior including regular (tonic) spiking, spike bursts, Ca^{2+}-spikes and backpropagating action potentials (Hay et al., 2011).

---

[3] http://senselab.med.yale.edu/modeldb/ShowModel.asp?model=139653

Table 1
Default parameters for conductance-based synapses.

Symbol	Unit	Description	Excitatory	Inhibitory
E_E, E_I	mV	Reversal potential	0	−80
$g_{max,E}, g_{max,I}$	μS	Max. conductance	0.0125	0.025
$\tau_{rise,E}, \tau_{rise,I}$	ms	Rise time-constant	1	1
$\tau_{decay,E}, \tau_{decay,I}$	ms	Decay time-constant	3	12
ρ_E, ρ_I	μm^{-2}	Synapse density	45 ± 4.5	20 ± 2.0

To achieve more heterogeneity in the simulated neuron populations, we utilized several parameter sets that in Hay et al. (2011) all were found to reproduce essential features of the perisomatic behavior, meaning generation of action potentials (APs). Two reconstructed morphologies were employed (Fig. 3a and b), with corresponding model-neuron description files and channel conductances, including passive membrane parameters, and three choices of model parameters (cf. Table 3, Tables S1 and S2 in Hay et al. (2011)) resulting in six possible combinations of channel conductances and morphologies. Although these particular models were not constrained to reproduce extracellular potentials, the resulting distributions of transmembrane currents during AP events gave plausible extracellular spike waveforms in terms of shape and amplitudes (cf. Section 3.1).

For the investigation of single-cell spike waveform variability, the morphology shown in Fig. 3a combined with the model parameters in Table 3 of Hay et al. (2011), was used. In the population studies we randomly selected neurons from the six possible combinations of morphology and model parameters.

Synapses. Conductance-based excitatory (AMPA) and inhibitory (GABA$_A$) synapses were modeled as a 'difference of two exponentials' (Roth and van Rossum, 2009). Excitatory synapses were distributed on dendritic segments only, inhibitory synapses were assigned to both dendrites and soma. We obtained plausible amplitudes of single-input postsynaptic potentials, i.e., up to ~ 9 mV for excitatory synaptic inputs onto proximal dendrites, and also reasonable overall firing rates ($\sim 0.3 - 20$ s^{-1}) when the neurons were subjected to continuous synaptic drive (see Appendix A). This was achieved by (1) manually specifying the mean synapse densities per membrane area (ρ_E, ρ_I, 10 % standard deviation) and drawing the number of synapses of each type from a normal distribution, (2) positioning each individual synapse randomly across segments with probabilities normalized according to target surface area, (3) adjusting the maximum conductances ($g_{max,E}, g_{max,I}$), and (4) setting synapse reversal potentials (E_E, E_I) and synapse rise/decay time constants ($\tau_{rise,E}, \tau_{rise,E}, \tau_{decay,E}, \tau_{decay,I}$) similar to Hendrickson et al. (2011). The synapse parameters are summarized in Table 1.

Population input from network. The incoming synaptic spike times to the postsynaptic population corresponded to spikes generated by a structured two-population spiking neuron network (Kriener et al., 2009), i.e., spike times of excitatory and inhibitory neurons from the network were employed as event times for excitatory or inhibitory synapses, respectively, reminiscent of the approach in Lindén et al. (2011). Thus the synaptic drive onto the spike-generating neurons was determined by the dynamics of the two-population spiking network. For the full network description, see Appendix A and Kriener et al. (2009). Alternatively (when noted), synapse activation times were generated using stationary Poisson processes with a fixed rate of 10 s^{-1}.

Cortical populations. We assigned somatic locations for all N neurons in each population within cylindric volumes with height $h_{cylinder}$ and radius $r_{cylinder}$. The cylinders were aligned with the axis of the recording device (the vertical z-axis). All neurons were placed with their somas in z-locations between the outmost contact points. Individual cell locations were set randomly using an iterative procedure with the following constraints: a minimum
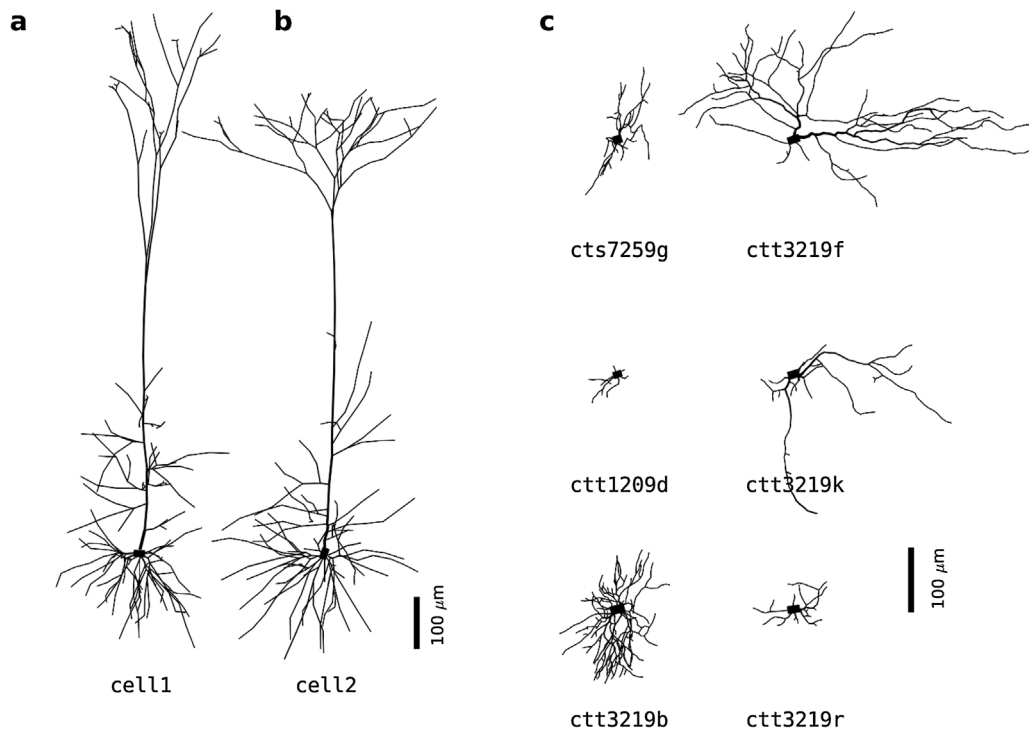
Fig. 3. Neuron morphologies used to generate benchmarking data. (a, b) Morphologies of the layer 5b pyramidal cell models from Hay et al. (2011) used to generate benchmarking data mimicking in vivo tetrode and polytrode recordings. (c) Subset of retinal ganglion cells (RGCs) used to generate benchmarking data mimicking in vitro retinal MEA recordings, taken from Sheasby and Fohlmeister (1999).

Table 2
Main simulation parameters for electrodes and populations for each set of benchmarking data.

Symbol	Unit	Description	Tetrode	Polytrode	MEA
σ_e	S m^{-1}	Conductivity	0.3	0.3	0, 0.1, 1.5
$n_{contacts}$		Number of contacts	4	16	102
$r_{contacts}$	μm	Contact point radius	7.5	7.5	7
N		Number of cells	6	16	56
$r_{cylinder}$	μm	Outer population radius	50	50	–
$h_{cylinder}$	μm	Population height	150	750	–
d_{ss}	μm	Min. soma-to-soma distance	25	25	–
dt	ms	Time resolution	0.03125	0.03125	0.03125
f_s	Hz	Sampling frequency	32 000	32 000	32 000
n_{bumps}		Cosine bump count	16	16	16
n_{taps}		Filter length	401	401	401
α		Log-bump param.	0.01	0.01	0.01

soma-to-soma inter-distance of d_{ss} = 25 μm (as computed from the center of each soma segment), and minimum proximity of somatic segments of 25 μm to the volume occupied by the recording device, i.e., electrode shaft (cf. Section 2.2). Neurons were aligned with their apical dendrite parallel to the z-axis, with a random rotation. As dendritic segments typically contribute less to the extracellular potential than their somatic counterpart (Lindén et al., 2010), we here allowed dendritic sections to lie within the volume occupied by the electrode, however, dendrites were not allowed too close to the electrode contacts themselves, see Section 2.5. Population parameters are summarized in Table 2. The benchmarking data mimicking *in vivo* results discussed here was obtained with the locations of each neuron and contact points fixed throughout simulations. However, ViSAPy is also able to emulate vertical electrode drift by shifting the z-locations of the electrode contact points in fixed steps at regular time intervals.

2.4. In vitro retinal data for microelectrode arrays (MEAs)

For MEA benchmarking data we emulated salamander retinal-slice recordings, the subject matter of several recent studies, e.g.,

Table 3
Default spiking neuron network parameters.

Symbol	Unit	Description	Value
h	ms	Temporal resolution	0.03125
N_E		Number of excitatory cells	10 000
N_I		Number of inhibitory cells	2500
τ_{mem}	ms	LIF neuron time constant	20
τ_{refr}	ms	LIF neuron refractory period	2.0
θ_{spike}	mV	LIF neuron firing threshold	20
V_{res}	mV	LIF neuron reset potential	0
κ		Number of connections	1250
g		Excitatory/inhibitory weight ratio	5.0
Δ	ms	Transmission delay	2.0
J_E	mV	EPSP amplitude	0.05
J_I	mV	IPSP amplitude	$-gJ_E$
J_{noise}	mV	EPSP of stat. Poissonian noise	0.05
$J_{ext.noise}$	mV	EPSP of non-stat. Poissonian noise	0.5
υ_{noise}	Hz	Stationary Poisson process rate	900
$\upsilon_{ext.noise}$	Hz	Non-stat. Poisson processes rate	40
$n_{ext.noise}$		Number of non-stat. Poisson proc.	$N_E + N_I$
Δ_{noise}	ms	Transmission delay non-stat. Poisson proc.	h
μ_n	rad	Center of von Mises distribution, cell n	$\frac{2\pi n}{N} - \pi$
κ_n	rad$^{-\frac{1}{2}}$	Dispersion of von Mises distribution	π

Segev et al. (2004, 2006). A set of 53 biophysically detailed models of salamander retinal ganglion cells were utilized (Sheasby and Fohlmeister, 1999), where the corresponding model files were downloaded from ModelDB.[4] A subset of corresponding neuronal reconstructions are shown in Fig. 3c. Salamander retinas have retinal ganglion cell layers with a cell density on the order of 1400 cells per mm^2 (Segev et al., 2004, 2006). With an ordered hexagonal organization as used here, this density corresponds to a mean cell spacing of 29 μm. Random offsets with a standard deviation of ± 5 μm were applied to each cell's location along both planar axes. Each cell was chosen randomly from the 53 available models.

In the MEA setup, the retinal slice is placed onto the MEA chip and covered with saline (Ness et al., 2015). Both the electrical conductivity in the slice and the typical distance of the retinal ganglion cells from the MEA chip plane, each needed for forward-modeling of MEA potentials (cf. Section 2.5 and Ness et al. (2015)), are not accurately known. They were thus set as follows: The average height of the somas above the electrode plane were adjusted such that the model reproduced experimentally observed spatial attenuation of spike amplitudes when moving laterally in the electrode plane, i.e., a spatial exponential decay constant of ∼ 28 μm (Segev et al., 2004). This procedure predicted an average soma to MEA-plane distance of 15 μm. We thus placed the somas at an average vertical heights of 15 μm, but to allow some jitter we added a random Gaussian spread with a standard deviation of 1 μm. Further, the electrical conductivity in our 200 μm thick retinal model slice was adjusted such that the spike amplitudes were comparable to experimental observations also in Segev et al. (2004) resulting in a tissue conductivity of 0.1 S m^{-1}.

The model retinal ganglion cells were activated by a simplified model for a graded synaptic input current (Palmer, 1999), in the form of a time-varying synaptic conductance onto their somatic compartments given by $I_{syn}(t) = g_{syn}(t)(V_{soma} - E_E)$. For each cell, we created uncorrelated signals using a mean-reverting Ornstein–Uhlenbeck process (Uhlenbeck and Ornstein, 1930; Tuckwell et al., 2002). Next, we assumed an exponentially decaying soma-to-soma distance-dependence of the correlation of each signal using the form $\exp(-d/\lambda_d)$, where d is the distance between each cell pair and $\lambda_d = 29$ μm was chosen as space constant (similar to the mean cell spacing), in order to have a higher probability of temporally overlapping spike waveforms generated by cells in close proximity of each other. We made the signals correlated by first computing the Cholesky decomposition factor (see Section 2.6) of the of the input correlation matrix, which in turn was multiplied with the matrix containing the uncorrelated signals. The output, representing the synapse conductance $g_{syn}(t)$ in each individual cell, was scaled and shifted to have a mean value and standard deviation of $2.00 \pm 1.33 \times 10^{-1}$ S m^{-2} in order to make all cells in the population generate action potentials (at rates of ∼ 6 − 30 Hz).

2.5. Forward models for extracellular potentials

From volume conductor theory it follows that under the assumption of an infinite, electrically linear and homogenous conductive media, the contribution to the electrical potential measured by a (virtual) point electrode positioned at $\vec{r}$ is given by (Holt and Koch, 1999; Lindén et al., 2014):

$$\Phi\left(\vec{r}, t\right) = \frac{1}{4\pi\sigma_e} \frac{I_0(t)}{|\vec{r} - \vec{r}_0|}, \tag{1}$$

where $I_0(t)$ denotes a point current source positioned at $\vec{r}_0$. This formula represented the basis for the generation of our *in vivo*

benchmark data (i.e., tetrode and polyelectrode), and a scalar conductivity $\sigma_e = 0.3$ S m^{-1} was used (Hämäläinen et al., 1993, but see Goto et al., 2010). In the presently used *line-source approximation* (Holt and Koch, 1999; Gold et al., 2006, 2007, 2009; Pettersen et al., 2008; Lindén et al., 2010, 2011, 2014) each dendritic segment is represented as a line source with evenly distributed currents, and for N multicompartmental model neurons, each discretized into n_j segments, the extracellular potential contribution is obtained by integrating Eq. (1) along each segment i of each cell j:

$$\Phi\left(\vec{r}, t\right) = \sum_{j=1}^{N} \sum_{i=1}^{n_j} \frac{I_{j,i}(t)}{4\pi\sigma_e} \int \frac{1}{|\vec{r} - \vec{r}_{j,i}|} d\vec{r}_{ji}. \tag{2}$$

Here, $I_{j,i}(t)$ is the transmembrane current of segment i of neuron j, $\vec{r}$ the location of the recording electrode contact, and $\vec{r}_{j,i}$ the location of the segment. A simple formula found from evaluating the integral Eq. (2) (see, e.g., Eq. (4) in Lindén et al., 2014) was used to compute the contribution from each line segment. As the soma segment may more realistically be approximated as a spherical current source if its length-to-diameter ratio is approximately 1, we combined the point-source approximation for the soma (Eq. (1)) with the line-source approximation (Eq. (2)) for the dendritic segments to obtain (Lindén et al., 2014):

$$\Phi(\vec{r}, t) = \sum_{j=1}^{N} \frac{1}{4\pi\sigma_e} \left(\frac{I_{j,soma}(t)}{|\vec{r} - \vec{r}_{j,soma}|} + \sum_{i=2}^{n_j} \int \frac{I_{j,i}(t)}{|\vec{r} - \vec{r}_{j,i}|} d\vec{r}_{j,i} \right)$$
$$= \sum_{j=1}^{N} \frac{1}{4\pi\sigma_e} \left(\frac{I_{j,soma}(t)}{|\vec{r} - \vec{r}_{j,soma}|} + \sum_{i=2}^{n_j} \frac{I_{j,i}(t)}{\Delta s_{j,i}} \log \left| \frac{\sqrt{h_{j,i}^2 + \rho_{j,i}^2} - h_{j,i}}{\sqrt{l_{j,i}^2 + \rho_{j,i}^2} - l_{j,i}} \right| \right). \tag{3}$$

Here $\Delta s_{j,i}$ denotes compartment length, $\rho_{j,i}$ the perpendicular distance from the electrode point contact to the line compartment, $h_{j,i}$ the longitudinal distance from one end of the compartment, and $l_{j,i} = \Delta s_{j,i} + h_{j,i}$ the longitudinal distance from the other compartment end. If the distance between electrode contact and a dendritic current source accidentally gets very small, i.e., smaller than the radius of the dendritic segment, an unphysical singularity in our line-source potential may occur. In these cases singularities are avoided by setting $\rho_{j,i}$ equal to the dendritic compartment radius. Similarly for the point-source term (soma), we set $|\vec{r} - \vec{r}_{j,soma}|$ equal to the soma compartment radius if the distance is smaller than the soma radius. Contacts of real recording electrodes have finite spatial extent and are not point contacts as assumed above. However, the recorded signal can be well approximated as the mean of the potential across the uninsulated surface (Robinson, 1968; Nelson et al., 2008; Nelson and Pouget, 2010; Ness et al., 2015), at least for source distances further away than an electrode-contact radius or so (Ness et al., 2015). Here we employed this *disc-electrode approximation* (Camuñas Mesa and Quiroga, 2013; Ness et al., 2015), i.e.:

$$\Phi_{disc} = \frac{1}{A_s} \iint_S \Phi(\mathbf{u}, 0) d^2 u \approx \frac{1}{m} \sum_{i=1}^{m} \Phi(\mathbf{u}_i, 0), \tag{4}$$

and averaged the point-contact potential in Eq. (3) over $m = 100$ random locations across the contact surface S, A_S being the surface area. The chosen locations were distributed with uniform probability on circular disks representing each contact surface, with surface vectors oriented perpendicular to the electrode axis (or MEA plane) (Lindén et al., 2014). Calculations of extracellular potentials were facilitated by LFPy[5] (Lindén et al., 2014), in which NEURON is used for calculations of transmembrane currents (Hines et al., 2009).

In the MEA setup for *in vitro* slices the different electrical conductivities of the MEA chip, retinal slice, and saline bath imply

---

that the assumption of an infinite homogeneous volume conductor is violated. However, as shown in Ness et al. (2015), the *Method of Images* (MoI) from electrostatics (Barrera et al., 1978) can be adapted to accurately approximate the electrostatic forward solution of electric potentials resulting from transmembrane currents, see Appendix B. In the simulations we assumed a fully insulating MEA chip ($\sigma_e = 0$) and a tissue conductivity of $\sigma_e = 0.1\,\mathrm{S\,m}^{-1}$ in the 200 μm thick retinal slice (see Section 2.4). For the saline bath a conductivity of $\sigma_e = 1.5\,\mathrm{S\,m}^{-1}$ was used (Nunez and Srinivasan, 2006; Logothetis et al., 2007; Ness et al., 2015).

2.6. Background noise

In real extracellular recordings, numerous sources of noise (electronic noise, line noise, spikes from neurons far away) add to the recorded extracellular potentials (Martinez et al., 2009; Lindén et al., 2011; Thorbergsson et al., 2002; Camuñas Mesa and Quiroga, 2013). To incorporate realistic noise in our benchmark data, we thus developed a descriptive noise model that mimicked experimentally obtained signals in terms of frequency content, amplitude, and frequency-dependent covariance between recording channels. This synthesized noise was then added to the computed extracellular potentials from the spiking model population. From 15 s excerpts of *in vivo* mouse visual cortex recordings (see Section 2.1) and *in vitro* mouse retinal recordings obtained with a Hierlemann MEA (Frey et al., 2009, 2010; Hierlemann et al., 2011; Fiscella et al., 2012), each with n_contacts contacts (i.e., tetrode, polytrode, MEA), we concatenated signals with major spike events removed, using a detection threshold of five times the signal standard deviation of band-pass filtered data. A high spike-detection threshold was chosen as we found that removal from the signal of a large number of putative spikes identified by a lower threshold, had unwanted effects on the low-frequency parts of the noise. We then extrapolated the *power spectral density* (PSD) in each channel by Welch's average periodogram method (the fast Fourier transform (FFT) window length was 2^{16}, Hanning window function). A complex-valued matrix was subsequently constructed, corresponding to the desired number of output channels n_contacts, duration and time resolution of our extracellular potential simulations in the Fourier domain. Each matrix contained the product between each corresponding PSD magnitude and a complex exponential $\exp(i\theta)$, θ being a uniformly distributed random phase angle on the interval $[0, 2\pi\rangle$. After applying an inverse discrete Fourier transform operation on the matrix, we obtained n_contacts of uncorrelated noise signals with PSDs similar to real noise. To introduce correlations between the channels, both experimental and uncorrelated model noise signals were frequency resolved by a series of n_bumps filter basis functions represented as raised cosine 'bumps', on the form:

$$b_i(f) = \frac{\cos(\log(f + \alpha) - \eta_i) + 1}{2}, \tag{5}$$

so that for the frequency f we have that $\log(f + \alpha) \in [\eta_i - \pi, \eta_i + \pi\rangle$ and 0 otherwise (Field, 1987; Pillow et al., 2008). α was a chosen 'stretch' parameter, and the bump positions η_i distributed so that the basis vectors summed to 1. The first bump was a half-bump, and each equivalent filter was applied as discrete filters of length n_taps. These parameters for the raised cosine bump filters are summarized for each set of benchmark data in Table 2. The Cholesky decomposition factors of the covariance coefficient matrices between electrode channels were calculated for each frequency band of the real noise, and multiplied with the corresponding frequency-resolved model noise. The cross-channel correlated frequency bands were then superimposed with each other, yielding multi-channel artificial noise with comparable PSD and frequency-resolved cross-channel covariance similar to experimental data.

2.7. Benchmarking data analysis

Following standard procedure to facilitate detection of spike events from experimental data, we employed a two-step filtering procedure on the computed extracellular potentials, by (1) applying causal 1st order Butterworth band-pass filters with cutoff frequencies [0.5, 8000] Hz for DC and sampling alias removal, and (2) applying acausal 4th order Butterworth band-pass filters with cutoffs [300, 5000] Hz.

The ground-truth spike times of all neurons were assessed from the simulated somatic membrane potentials. An action-potential detection threshold of −30 mV was used (well above t-type Na⁺-channel activation), and the time step with the maximum slope during spike onset was chosen as the ground-truth spike time. The fast sodium current influx during action potential onset determines the peak of the extracellular spike waveform measured in proximity to the soma (Henze et al., 2000; Gold et al., 2006; Pettersen and Einevoll, 2008). Ground-truth inter-spike interval (ISI) histograms were calculated for ISI intervals between 1 and 1000 ms in 100 log-linear bins, unless stated otherwise.

To analyze the confidence of which model recordings could be sorted, we used the available ground-truth spike times for spike detection, thus avoiding the detection and alignment problem (Lewicki, 1998). The Python SpikeSort package (http://spikesort.org) was used to cut and temporally align waveforms according to the time of the peak amplitudes. Each spiking event was cut as $n_\text{channels} \times$ 100 time steps (i.e., 3.2 ms), offset by −20 time steps from the ground truth spike time. The tool was also used to compute *principal components* (PCs) of observed waveforms across electrode channels (Quiroga, 2007).

Spike-train correlations were computed from spike-time histograms with 10 ms bin widths, using the definition of the Pearson product-moment correlation coefficient, defined as

$$r_{ij} = \frac{\tilde{c}_{ij}}{\sqrt{\tilde{c}_{ii}\tilde{c}_{jj}}} = \frac{E[(x_i - \mu_{x_i})(x_j - \mu_{x_j})]}{\sqrt{E[(x_i - \mu_{x_i})^2]E[(x_j - \mu_{x_j})^2]}}, \tag{6}$$

where $\tilde{c}_{ij}$ is the covariance between the spike-time histograms x_i and x_j for two cells i and j, respectively, $\tilde{c}_{ii}$ the variance of x_i, E the expectation (i.e., the mean), and μ_{x_i} the mean of x_i, and similar for x_j (Tetzlaff and Diesmann, 2010).

3. Results

3.1. Single-cell spike waveform variability

Before embarking on the generation of benchmarking data from neural populations, we here first investigate generic issues related to spikes and, in particular, spike waveform variability. In Fig. 4a we show spike waveforms at various positions around the soma of a L5b pyramidal cell model taken from Hay et al. (2011). Here the action potential was generated without explicit synaptic inputs, but rather by raising the reversal potential of the passive leak channel across the neuron. An immediate observation is that the spike waveform depends strongly on position, in particular its amplitude (see color code), but also the shape (see, e.g., the spikes recorded above the soma close to the apical dendrite). As expected the largest spikes can be found close to the soma, and here the characteristic shape with a sharp negative 'sodium spike' followed by a longer positive 'potassium bump' is observed (Henze et al., 2000). Spike waveforms recorded close to the thick apical dendrite have a different shape with a fast positive peak due to capacitive currents preceding the sodium spike and potassium bump. These observations are in agreement with previous studies (Holt and Koch, 1999; Gold et al., 2006, 2007; Pettersen and Einevoll, 2008).
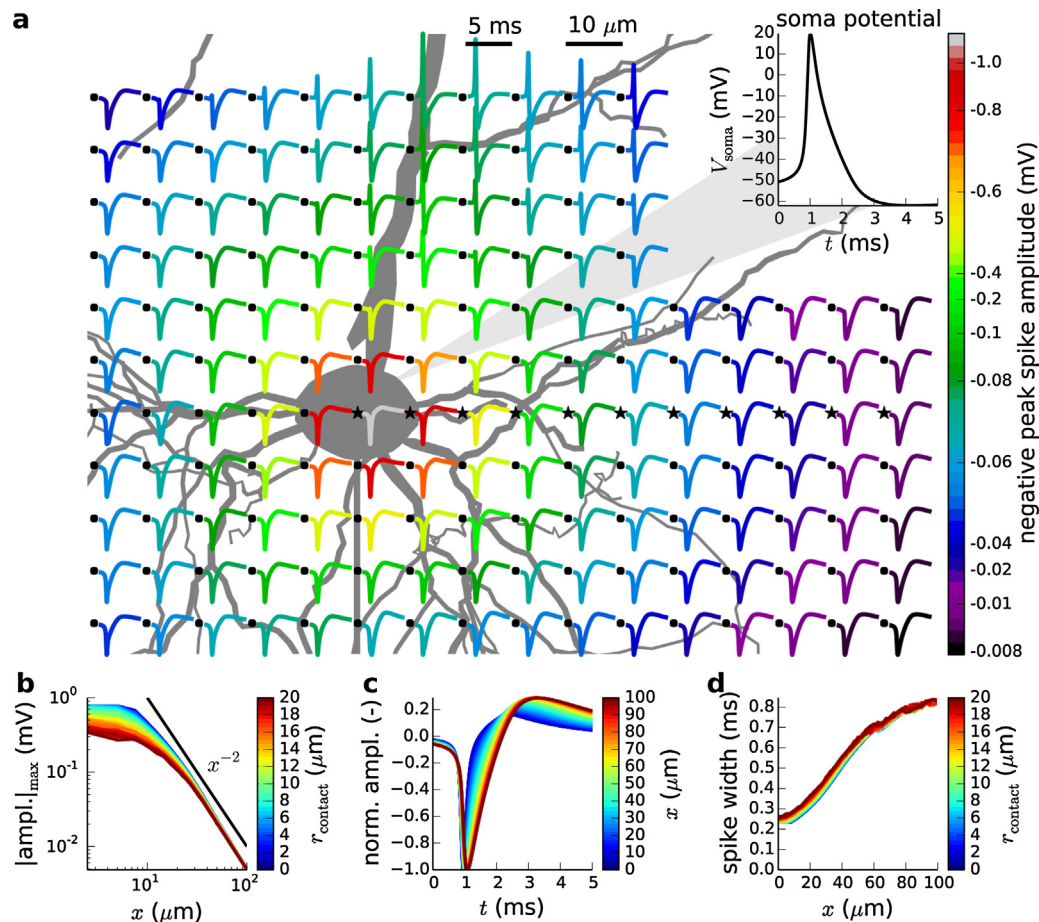
Fig. 4. Position-dependent spike waveforms and effects of contact size for a L5b pyramidal model neuron. (a) Normalized spike waveforms color coded to their negative peak amplitude for a set of in-plane positions (for a plane passing through the soma center) superposed on neuronal morphology. Intracellular action potential shown in upper right inset. (b) Dependence of maximum absolute extracellular spike amplitude on lateral distance x and contact radius $r_{contact}$. (c) Spike waveforms normalized to the negative peak as a function of distance along x-axis with fixed electrode contact radius $r_{contact}$ = 7.5 μm. (d) Spike width, defined as width of trough at 50% min-max amplitude difference, as function of lateral distance and contact point radius. In panels (b–d), spike amplitudes and spike widths were along x-axis locations marked with asterisks in panel (a). The chosen morphology and corresponds to the morphology `cell 1` depicted in Fig. 3a while model parameters corresponds to the set listed in Table 3 in Hay et al. (2011). The action potential was generated by increasing the reversal potential of the passive leak channel from the default value of −90 mV to −59.7 mV. (For interpretation of the references to color in this figure legend, the reader is referred to the web version of the article.)

3.1.1. Effect of electrode contact size

The results in Fig. 4a are for an ideal point-electrode contact. Real electrodes of course have physical extensions, and in Fig. 4b we illustrate how the amplitude of the recorded spike depends on electrode contact radius, $r_{contact}$, using the disc-electrode approximation in Eq. (4). Results are shown for recordings along a horizontal line extending out from the soma, see asterisks in Fig. 4a. Electrode contact radii up to 20 μm are considered, and for these we observe that the contact size has a substantial effect on the amplitude of the recorded spikes for the smallest lateral distances (i.e., $\lesssim$ 10–20 μm) from the soma center: larger contacts give smaller peak amplitudes as the averaging over large surfaces prevents a strongly dominant contribution from a current source placed very close to a small contact. Note, that the disc-electrode approximation itself will be inaccurate for the largest electrode contacts and shortest distances considered. However, comparison with results from Finite Element Modeling (FEM) (Larson and Bengzon, 2013) suggests that only for distances less than half the electrode radius or so will the error inherent in the approximation be larger than 10% (Ness et al., 2015).

In Fig. 4b we further observe that for lateral distances x approaching hundred micrometers, the amplitude decays roughly inverse with the square of the distance, i.e., as $1/x^2$, in accordance with the dominance of the current-dipole contributions in the

far-field limit (Pettersen and Einevoll, 2008; Pettersen et al., 2012). In addition to the amplitude, the spike shape also varies with lateral distance, cf. Fig. 4c. Here we see that the spikes recorded further away from the soma are blunter and wider (red) than spikes recorded very close (blue). We also observe that the spike widening is mainly due to increased delay of the positive 'potassium bump' with distance, the times of negative sodium peaks are only slightly delayed. In Fig. 4d the distance dependence of the spike width (see definition in figure caption) is quantified, and a monotonic increase is observed. This is in accordance with previous observation on other model neurons (Gold et al., 2006; Pettersen and Einevoll, 2008) and can be understood in terms of the *intrinsic dendritic filtering* effect where the high-frequency current dipole lengths are reduced compared to the low-frequency dipole lengths due to the capacitive properties of the neuronal membrane (Pettersen and Einevoll, 2008; Lindén et al., 2010; Pettersen et al., 2012). In this panel we also see that the electrode size has a marginal effect on the spike width for all distances considered.

3.1.2. Spike-shape variability from varying interspike intervals (ISI)

Several experimental studies have demonstrated spike waveforms that depend on the time since the previous spike, i.e., the *interspike interval* (ISI) (Fee et al., 1996; Quirk and Wilson, 1999;

Henze et al., 2000; Buzsáki, 2004; Stratton et al., 2012). Such wave-form variability poses a particular challenge on spike sorting and should thus be part of benchmarking data sets. For our model neuron in Fig. 4, a series of spikes induced by a fixed change of the passive leak reversal potential without any synaptic inputs, will (after a possible initial transient) display identical waveforms. However, when the neuron instead was driven with noisy synaptic inputs, a prominent ISI-dependence of the spike waveform was observed.

Fig. 5 illustrates the spike waveform dependence on the ISI for the model neuron in Fig. 4 when the neuron instead is driven by synaptic inputs (see figure caption for specification). Waveforms at three distances from the soma along the *x*-axis are considered: $x = 10 \mu m$, $50 \mu m$, and $100 \mu m$, respectively. Excerpts of the somatic membrane potential and the extracellular potentials at these three positions are shown in Fig. 5a, with corresponding power spectral densities (PSD) depicted in Fig. 5b. The most prominent feature is the strong decay of signal amplitude and power when moving for $x = 10 \mu m$ to $x = 100 \mu m$, i.e., two orders of magnitude for the signal (panel a) and four orders of magnitude for the power (panel b), respectively. We also note the sharper high-frequency decay in the PSDs of the soma membrane potential compared to the extracellular potential for the highest frequency, in accordance with previous findings (Pettersen and Einevoll, 2008; Pettersen et al., 2012, 2014; Lindén et al., 2010).

More importantly, Fig. 5c shows the combined ISI distribution from simulation of 32 different synaptic realizations (see caption) for a total duration of 120 s. A very broad ISI distribution is observed, stretching from a few milliseconds up to a full second. The ISI distribution is further seen to have a bimodal distribution with a first peak centered between 5 and 10 ms, in accordance with the bursting property (Le Bé et al., 2007) of the present model neuron (Hay et al., 2011). Fig. 5d shows that the intracellular action-potential (AP) waveform depends strongly on the ISI. Higher amplitudes both of the sodium depolarization peak and the later potassium after-hyperpolarization dip are associated with longer and intermediate ISIs. For the shortest ISIs corresponding to non-leading spikes in a burst, much blunter AP signatures are observed, in accordance with Hay et al. (2011) and Le Bé et al. (2007). This point is further highlighted in Fig. 5e showing an inverse correlation between the AP peak-to-peak amplitude and the AP signal width.

The same trend, i.e., weaker and blunter signals for short ISIs, is also seen for the extracellular waveforms: Fig. 5f illustrates the ISI-dependence of the raw spike waveform recorded very close to the soma ($x = 10 \mu m$), while Fig. 5g shows the same for band-pass filtered waveforms (mimicking filtering done in a typical experimental recording). The corresponding spike amplitude vs. spike width plot in Fig. 5j reveals a clear inverse relationship. The trend is still present for $x = 50 \mu m$ (Fig. 5k) but less distinct since the signal amplitudes are much smaller and the relative noise level much higher than for $x = 10 \mu m$. For $x = 100 \mu m$ a large waveform variability is still observed (Fig. 5l), but a clear relationship between spike amplitude and spike width can no longer be discerned. This observed inverse relationship between spike amplitude for spike widths observed for recording electrodes close to the soma, is in accordance with experimental findings (Harris et al., 2000). Henze et al. (2000) further found that increased intracellular action-potential amplitudes were associated with increased extracellular spike amplitudes, and this positive correlation is also present in our model data, i.e., large intracellular and extracellular spike amplitudes are both associated with large ISIs (cf. panels d–l).

The positive correlation between extracellular spike amplitude and time since the last spike is further illustrated in the amplitude vs. ISI plots in Fig. 5j–l, qualitatively similar to what was seen in the experiments of Fee et al. (1996) (and also in accordance with the observation of a systematic reduction of spike amplitude

during bursting, see Harris et al., 2000). These panels also highlight the considerable amplitude variability seen for the same ISI times, reflecting that the model neuron was targeted by a barrage of random Poisson-distributed synaptic inputs. In fact, occasionally we observed high-amplitude spikes preceded by smaller spikes even at short ISIs. This variability reflects continuously varying levels of membrane depolarization and effective membrane time constants due to fluctuating synaptic and intrinsic channel conductances (Destexhe and Paré, 1999; Destexhe et al., 2001).

The ISI-dependence of the spike waveform (both amplitude and shape) represents a major challenge for spike-sorting algorithms (Fee et al., 1996; Harris et al., 2000; Delescluse and Pouzat, 2006; Einevoll et al., 2012). This is illustrated in Fig. 6 where the spikes in Fig. 5 are recorded with a linear tetrode oriented in parallel with the thick apical dendrites (i.e., in the *z*-direction) with a lateral displacement of $20 \mu m$ from the soma center. The strong ISI-dependence of the spike waveforms recorded in the four channels (positioned at $z = 100 \mu m$, $50 \mu m$, $0 \mu m$, and $-50 \mu m$, respectively) is shown in Fig. 6a. Spike-sorting algorithms are based on clustering of particular features of the waveform (Einevoll et al., 2012), and principal components (PCs) are commonly used in combination with clustering algorithms assuming Gaussian-shaped clusters. In Fig. 6b we show the joint distributions of the two first PCs for each of the four channels, revealing strong non-Gaussian features. As seen from the color coding in these distribution plots, this non-Gaussianity largely stems from the ISI-dependence of the waveform. Several approaches have been tried to address this key challenge for spike sorters (Fee et al., 1996; Rinberg et al., 1999; Harris et al., 2000; Delescluse and Pouzat, 2006) and may be tested on such benchmarking data.

### 3.2. Benchmarking data mimicking tetrode recordings

3.2.1. Noise from experiments

To make benchmarking data mimicking *in vivo* spike recordings, we fitted a descriptive noise model (see Section 2.6) to experimentally recorded noise and later added this model noise to the extracellular potentials generated by the neuronal model population. Experimental recordings were done *in vivo* with a linear multielectrode in mouse visual cortex, and an excerpt from a recording on four neighboring contacts is shown in Fig. 7a. The data were preprocessed by removal of large-amplitude spike events and spurious frequency peaks in the power spectral density (PSD). The resulting signals were then used as experimental tetrode noise to be mimicked in a statistical sense by our noise model.

The PSDs shown in Fig. 7b reveal that even if low-frequency noise dominates, the noise also has substantial components at higher frequencies with a sharp decay of noise power in the frequency range relevant for spike detection, i.e., above a few hundred hertz (Pettersen and Einevoll, 2008). Another immediate observation is the very strong correlation between the noise signals in the four channels in Fig. 7a. Our descriptive noise model effectively captured these features by use of 16 raised cosine 'bump' filters covering different frequency bands (Fig. 7c) where the covariance structure between the four channels were estimated for each of the 16 filter bands separately (Fig. 7d). As seen here, the lowest frequencies, i.e., the lowest-numbered bump-filter frequency bands, show the highest correlation between the channels. The extracted information was sufficient to allow for the generation of synthetic noise with very similar appearance as the experimental noise: the model noise in Fig. 7e is essentially indistinguishable in its general appearance from the *in vivo* experimental noise in Fig. 7a.

3.2.2. Presynaptic spike trains driving model population

In Section 3.1.2 we found that irregular synaptic inputs onto a single model neuron produced ISI-dependent spike waveforms
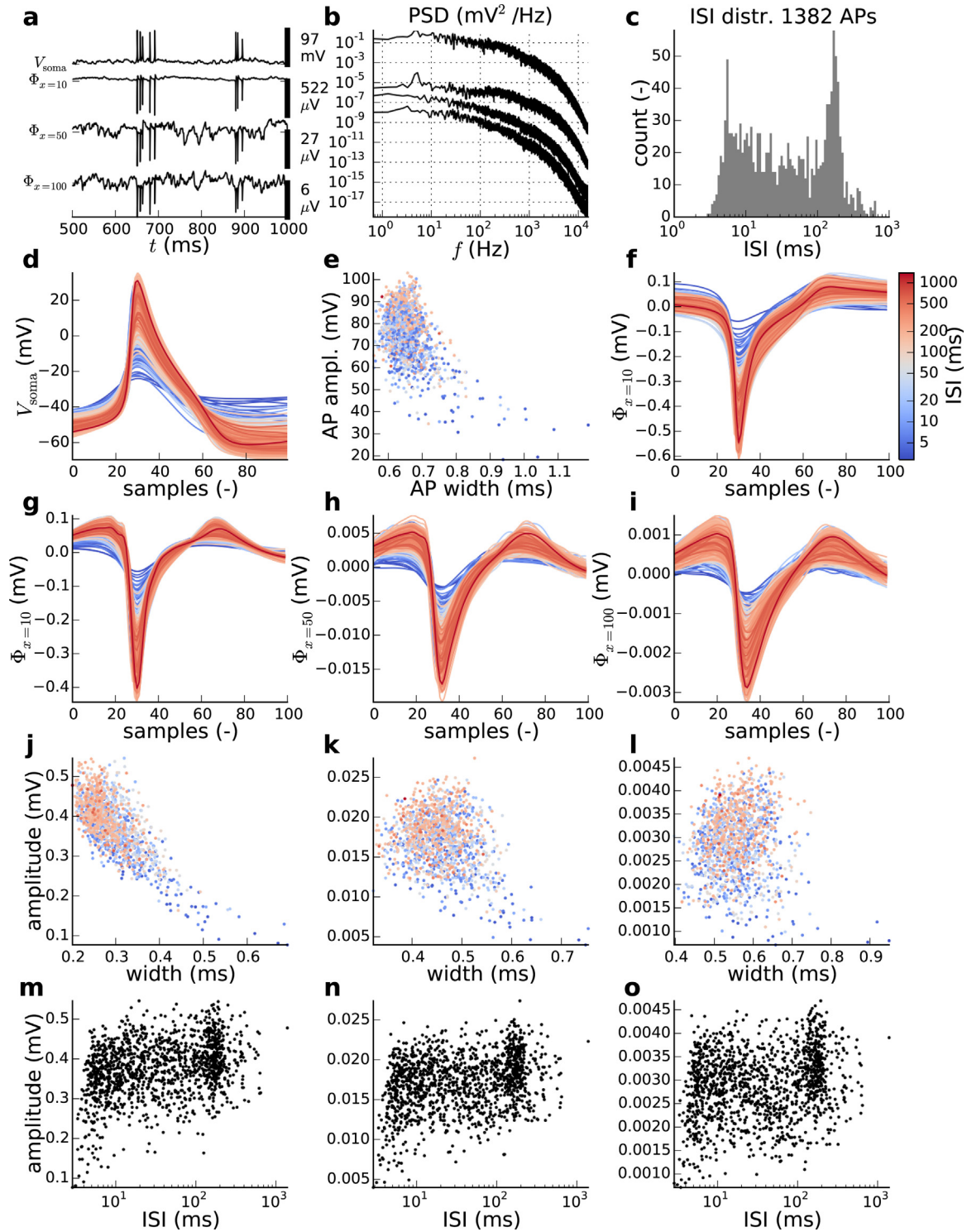
Fig. 5. Intrinsic spike waveform variability from a L5b pyramidal neuron receiving noisy synaptic inputs. (a) 500 ms excerpt of the soma membrane potential V_{soma} and extracellular potentials in contacts located in $x = [10, 50, 100]\,\mu m$ and $z = y = 0\,\mu m$ from the soma, with $r_{contact} = 7.5\,\mu m$. (b) Frequency content in V_{soma} (top trace) and extracellular traces (traces below in the order $x = 10, 50, 100\,\mu m$). (c) Interspike interval (ISI) distribution in log-linear bins of all spike events from 120 s total simulation time. (d) Detected AP waveforms, each trace color coded for corresponding ISI. (e) AP amplitudes defined as max–min-difference vs. AP widths calculated at 50% of this max–min difference computed for each AP waveform. (f) Raw extracellular spike waveforms proximally to soma ($x = 10\,\mu m$). (g–i) Band-pass filtered extracellular spike waveforms at $x = [10, 50, 100]\,\mu m$. (j–l) Projections of spike amplitudes vs. spike widths for $x = [10, 50, 100]\,\mu m$. (m–o) Spike amplitudes vs. interspike intervals (ISIs) for $x = [10, 50, 100]\,\mu m$. The neurons were driven with excitatory and inhibitory synapses (cf. Section 2.3) with increased density of excitatory synapses, $\rho_E = 47.5 \pm 4.75\,\mu m^{-2}$, compared to default values in Table 1. Each synapse received uncorrelated spike trains with Poisson statistics with rates $\upsilon_{noise} = 10\,s^{-1}$. 32 model realizations with unique synapse distributions (resulting from different random seeds and standard deviation in ρ_E and ρ_I) were simulated in parallel for a total duration of 120 s real time resulting in approximately 1400 sampled spike events. Somatic membrane potentials, raw and filtered extracellular potentials sampled as described in Section 2.7. (For interpretation of the references to color in this and subsequent figures and legends, the reader is referred to the web version of the article.)
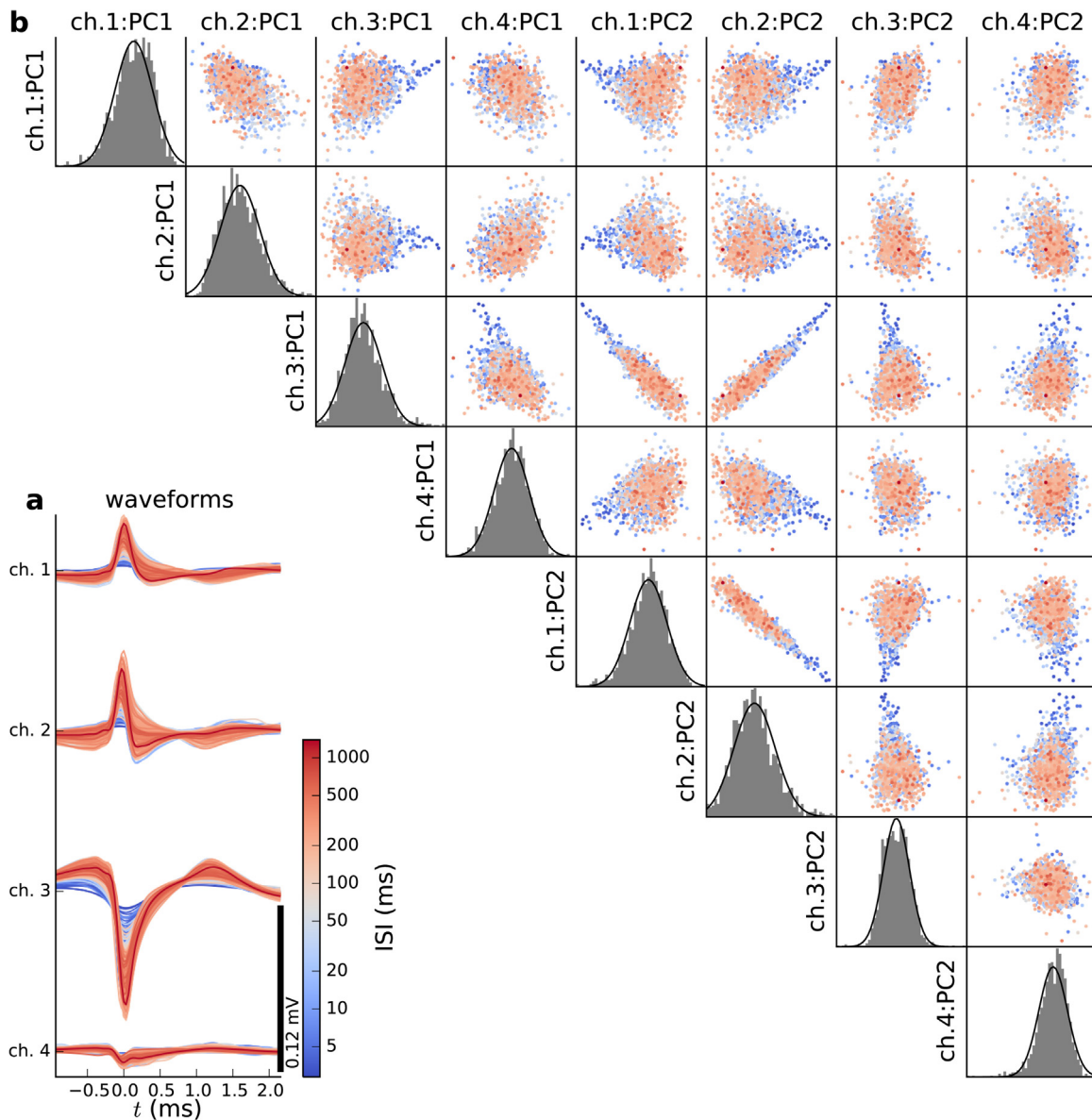
Fig. 6. Effect of ISI-dependent extracellular waveform variability on features used in spike sorting. (a) Band-pass filtered spike waveforms recorded by a linear tetrode oriented in the *z*-direction with a lateral displacement of 20 μm from the soma center. Channels 1–4 correspond to recordings by contact at $z = [100, 50, 0, -50]$ μm, respectively. Contact size: $r_{contact} = 7.5$ μm. (b) Projections and distributions of the first two principal components (PCs) across the four channels for the data in panel (a).

in accordance with what is seen in *in vivo* experiments. We also want to have the opportunity to control the level of correlations of synaptic inputs driving the different neuron models in our test population. While this could be achieved by different means, we employed a two-population spiking neuron network model with a ring topology where neighboring neurons on the ring naturally have more correlated spiking than neurons further apart (Kriener et al., 2009, 2014), cf. Section 2.3 and Appendix A. The presynaptic spike trains driving each of the postsynaptic neurons in our model population are then drawn from partially overlapping sections of the network topology so that the postsynaptic neurons receive varying levels of shared and intrinsically correlated synaptic inputs.

In Fig. 8 we illustrate this procedure for our tetrode example, which here has six pyramidal model neurons generating extracellular spikes. Raster plots of the presynaptic spike trains driving the six cells are shown for excitatory and inhibitory inputs in Figs. 8a and b, respectively. Note, the higher number of excitatory inputs compared to inhibitory inputs. The correlations between these presynaptic spike trains are shown in Fig. 8c (excitatory inputs),

Fig. 8d (inhibitory inputs), and Fig. 8e (excitatory and inhibitory inputs). In all three cases we see that the correlations between the synaptic inputs driving the same neurons is high (diagonals in matrix plots) and then decay with distance, i.e., train 2 (driving cell 2) is quite correlated with train 1 (driving cell 1) as their synapse activation times were drawn from overlapping regions of the network topology, while train 3 and train 1 are less correlated, etc. (Note that train 6 also is quite correlated with train 1 due to the ring topology.)

The resulting activity in the postsynaptic population of six model L5b pyramidal cells (Hay et al., 2011) (Fig. 3a and b) is described in Fig. 8f–i. In this example, the six model neurons were constructed by randomly combining one (of two) neuronal morphologies with one (of three) sets of ion-channel densities, cf. Section 2.3. In addition both the synaptic locations and synapse activation times (cf. Fig. 8a and b) were different. Excerpts of the soma membrane potentials of each neuron are shown in Fig. 8f displaying substantial sub-threshold fluctuations and irregular spiking at rates varying in the range ~ 2–$16\,\mathrm{s}^{-1}$. The spikes
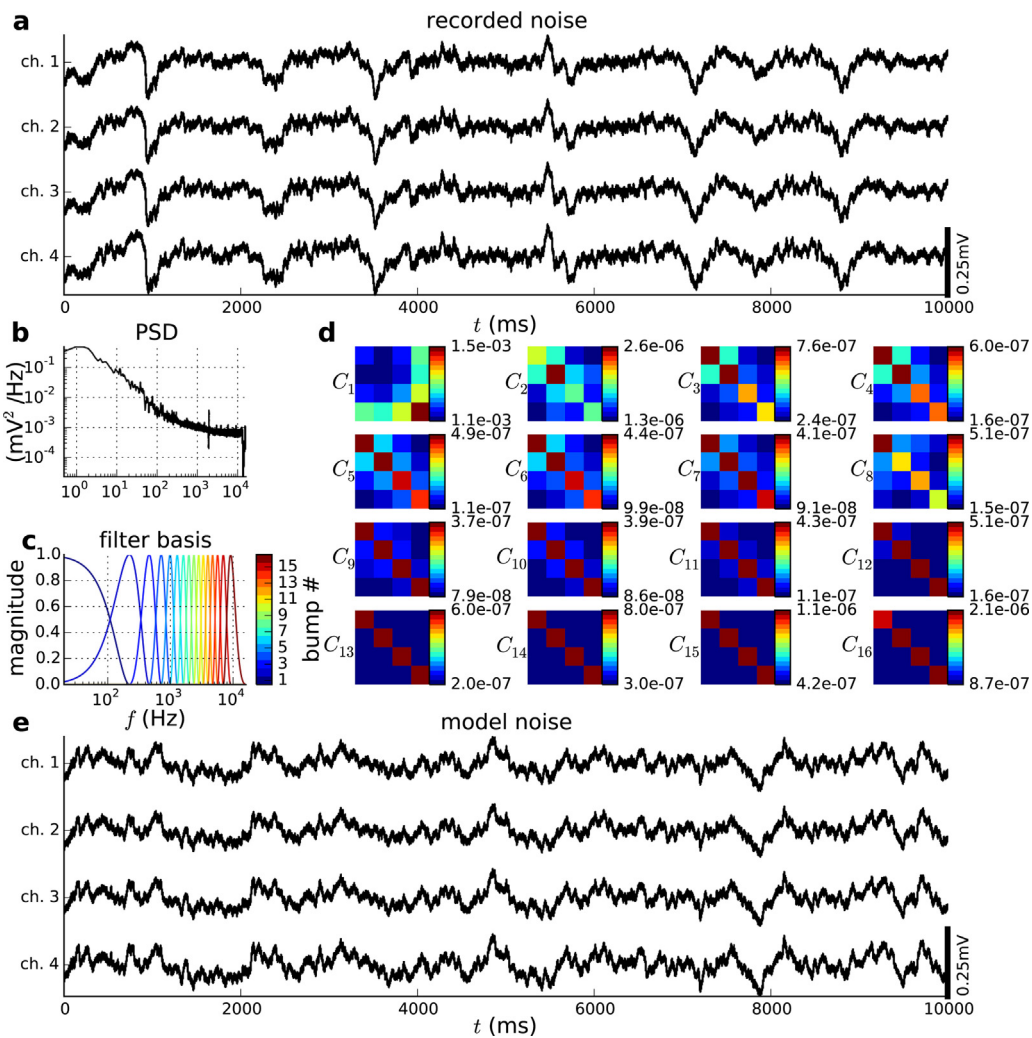
Fig. 7. Generation of synthetic noise similar to noise in in vivo cortical recordings. (a) In vivo recorded signals, treating four neighboring channels of a polytrode (linear multielectrode) as a virtual tetrode, here shown with high-amplitude spike events removed. (b) Power spectral density (PSD) extracted from the experimental traces averaged across channels. (c) Frequency response magnitudes of each discrete raised cosine 'bump' filter. (d) Cross-channel covariance matrices calculated for the in vivo experimental noise signals in the four channels for each of the 16 'bump' filter frequency bands. (e) Model noise generated with frequency-dependent covariance and PSD information extracted from in vivo tetrode recording.

extracted from these intracellular traces in our excerpt are shown in Fig. 8g, and the ISI distributions of all the spikes generated over a period of 120 s are shown in Fig. 8h. Here a large variation is seen among the six neurons: For example, while cell 4 had a high firing rate ($15.5\,s^{-1}$) and a clear bimodal ISI distribution with one of the peaks at less than 10 ms implying significant bursting behavior, cell 5 had a firing rate of only $2.5\,s^{-1}$ As seen in Fig. 8h this large variability between the neuronal firing patterns also seems to be reflected in weak cross-correlations in the spike times of the six postsynaptic neurons. Still, cells that received input from neighboring parts of the ring network were on average, if only barely, more correlated, i.e., compare, e.g., cell 1 vs. cell 2 and cell 1 vs. cell 4.
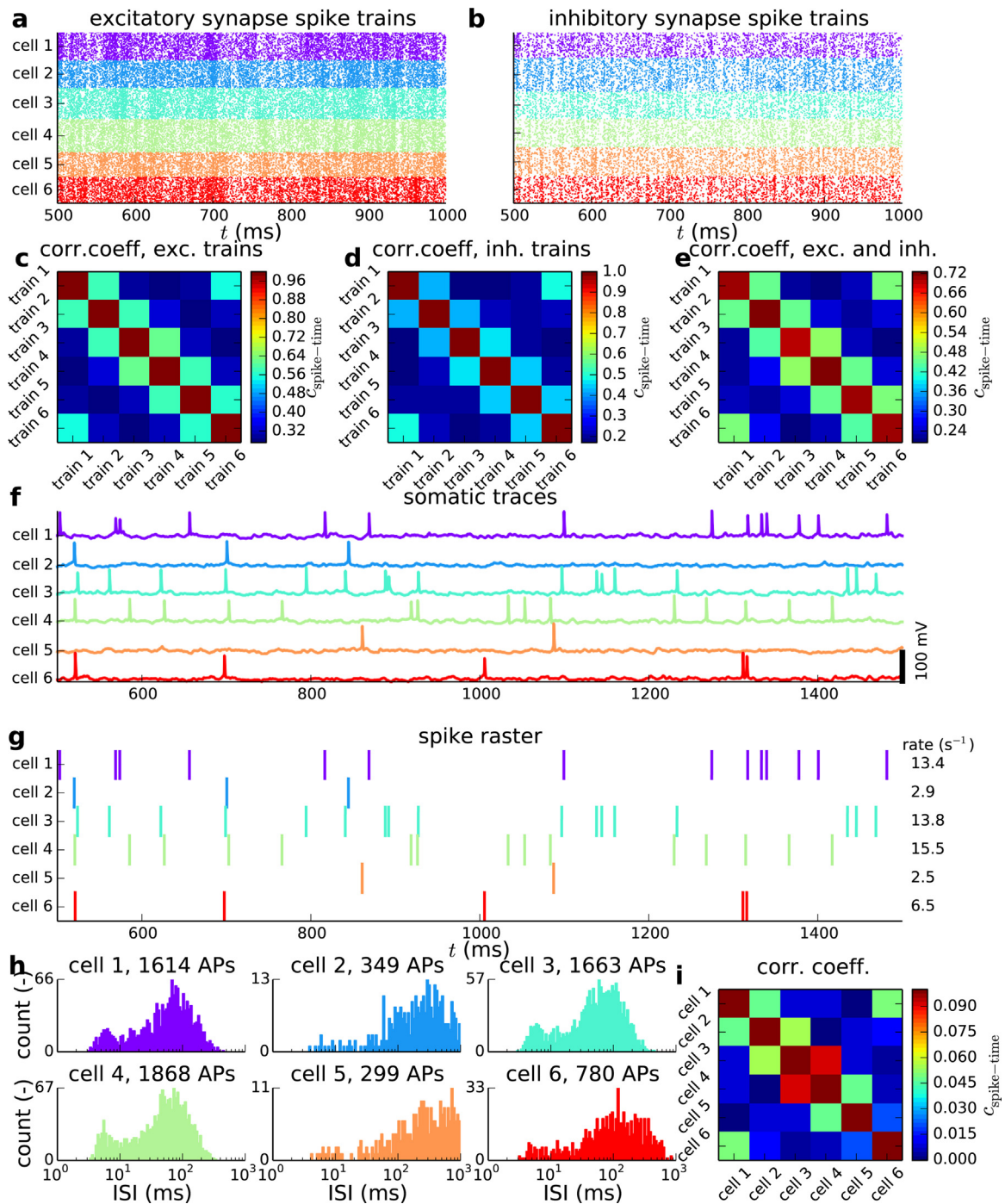
3.2.3. Tetrode benchmarking data

We now have all elements needed to construct our tetrode benchmarking data for *in vivo* recordings, and the results for a population of six pyramidal neurons with their somas placed within a radial distance of $50\,\mu m$ from an axis going through the linear array of electrode contacts (yet more than $25\,\mu m$ away from the volume occupied by the electrode shank), are shown in Fig. 9. The extracellular potentials generated by the neurons alone are seen in Fig. 9a to be much less noisy than typical *in vivo* data (as exemplified by the experimental noise recordings shown in Fig. 7a.)

However, with our synthesized model noise added (Fig. 9b), the signal looks biologically realistic. In spike-sorting applications, raw potentials recordings are typically band-pass filtered to remove low (and high) frequency signal components prior to spike detection, and the results from corresponding filtering of our compound model signals are shown in Fig. 9c. Again, the resulting signals looks similar to experimental data, see, e.g., Fig. 1a.

Fig. 9b (raw signals) and c (band-pass filtered signals) illustrates the type of benchmarking data that is produced by our biophysical modeling scheme. Here we know the ground truth about the spike trains, i.e., what neuron fired when, and in Fig. 9d we show the collection of spike waveforms for each neuron as recorded by the four channels as well as the averaged traces or *templates* (Einevoll et al., 2012). (This would correspond to the result from applying a perfect spike sorter, i.e., a sorter perfectly detecting and sorting the spikes, on our example data.) The observed spike amplitudes are typically $\lesssim 0.05\,mV$, i.e., similar to what is encountered in *in vivo* cortical recordings, see, e.g., Fig. 1. The absence of larger amplitudes was assured by our rule to enforce neurons to be positioned a certain minimum distance away from the recording electrodes (Section 2.3).

In Fig. 9e the respective templates are shown superimposed at the spike times of the source neurons on top of the (band-pass

Fig. 8. Network-generated synaptic inputs and resulting spiking outputs in neuronal population producing in vivo tetrode benchmarking data. The duration of the simulation was 120 s real time. (a) Synaptic spike trains activating excitatory synapses on the six cells in the postsynaptic population. Each row of dots corresponds to spikes from single neurons in the network providing synaptic input, and the colors denote postsynaptic target cells. (b) Corresponding spike trains activating inhibitory synapses. (c) Correlation coefficients (Eq. (6)) of excitatory synaptic input to each postsynaptic cell, calculated from spike-train histograms in 10 ms bins. 'train 1' refers to spikes driving synapse on 'cell 1', etc. (d) Same as (c), for binned spike trains activating inhibitory synapses. (e) Same as (c), for (pooled) binned spike trains activating both excitatory and inhibitory synapses. (f) Soma membrane potential of six cells in postsynaptic population. (g) Detected action potentials, i.e., the ground-truth spikes, for each postsynaptic cell with firing rates shown to the right. (h) Interspike interval (ISI) histograms in 100 log-linear bins for each cell. (i) Correlation coefficients between output spike trains, 10 ms temporal bin size. Note that upper color range value for reason of figure clarity has been set to 0.1, even if the autocorrelation coefficients (i.e., values on diagonal) by definition are 1. (For interpretation of the references to color in this figure and legend, the reader is referred to the web version of the article.)

filtered) signal. This figure also illustrates the problem caused by temporally overlapping spikes, e.g., the overlapping waveforms of cells 2, 3 and 6 around $t = 520$ ms.

Fig. 10, showing projections of the first two principal components of the measured waveform for the four channels, illustrates the large variability of the recorded spike shapes even when they

come from the same neuron. It further highlights that while some neurons form rather well-defined and well-isolated clusters, other neuron clusters show substantial overlaps, as was also seen in our example *in vivo* data in Fig. 1c. However, such overlaps can at least partially be resolved by projecting additional waveform features such as spike widths or peak-to-peak amplitudes (results not
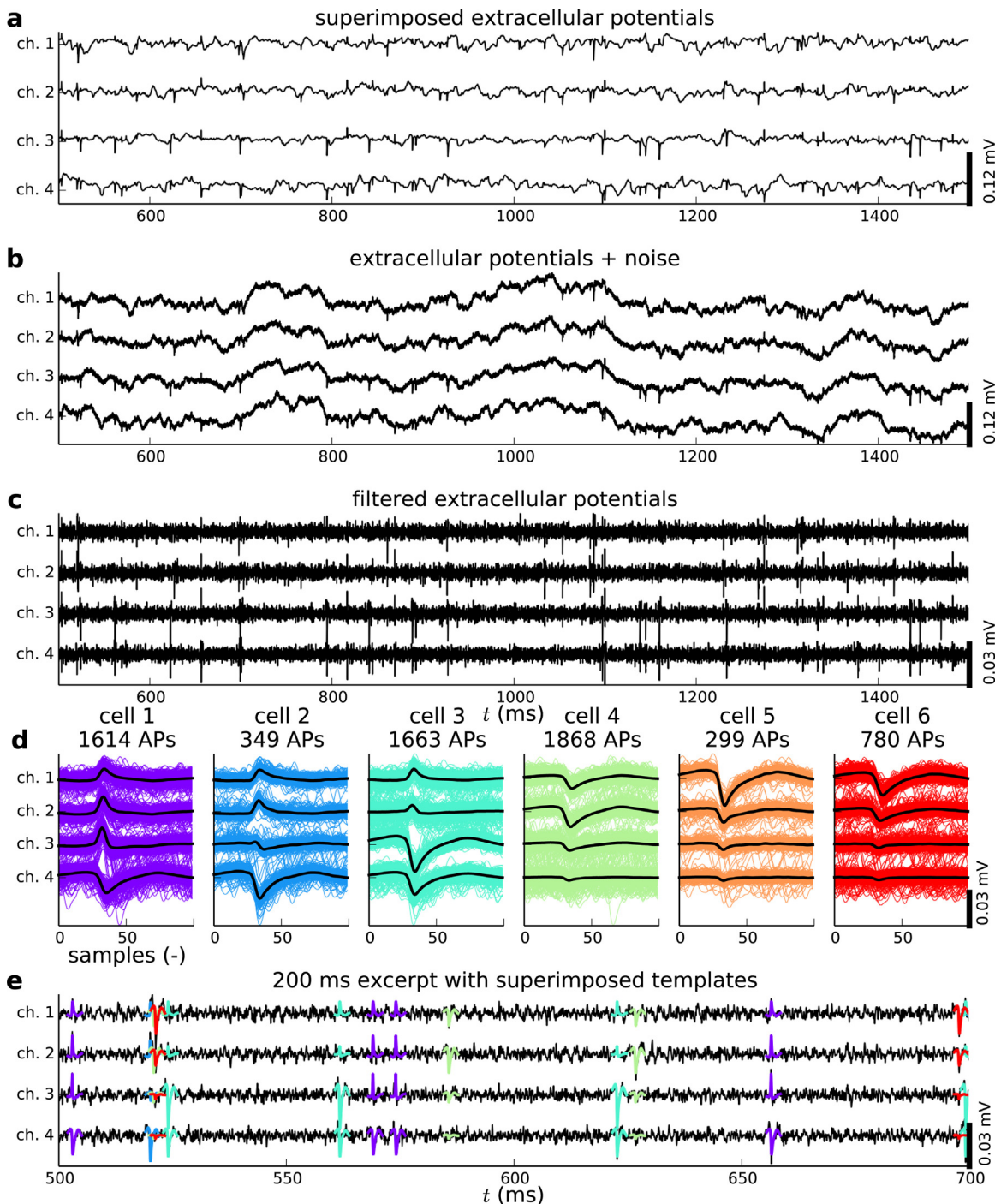
Fig. 9. Example benchmarking data for in vivo tetrode recordings. (a) Extracellular potential generated by population of six cortical pyramidal neurons in a simulation of 120 s real time. (b) Raw benchmarking data found from superposition of population potentials (from panel a) and synthesized model noise. (c) Filtered benchmarking data (corresponding to signals in (b)) facilitating spike sorting, see Section 2.7). (d) Collection of extracellular spike waveforms across channels for all neurons, with templates superimposed, i.e., per cell averaged spike waveforms. (e) Excerpt of band-pass filtered extracellular potentials with templates superimposed at corresponding spike events.

shown). A few outliers are seen in Fig. 10, and such outliers can be expected to occur with temporally overlapping spikes where the extracted waveforms become substantially distorted, cf. Fig. 9e.

3.3. Polytrode benchmarking data

As a second demonstration case, we consider benchmarking data for a 16 channel polytrode with 50 μm contact spacing, i.e., the type of multielectrode used to measure the present *in vivo* experimental data, cf. Section 2.1. The same procedure as for the tetrode data was used to fit our noise model to data, except that here 16 rather than four channels were used. As for the tetrode benchmarking data, layer 5b pyramidal cell models from Hay et al. (2011) were used, with the number of spiking neurons increased from 6 to 16 reflecting the larger vertical extension of the polytrode. As for the tetrode above, each cell was positioned less than 50 μm away from an axis going through the electrode contacts, yet at least 25 μm away from electrode shaft. Further, synaptic activation was provided by inputs from the two-population spiking ring network. A one-second sample of the resulting example benchmarking data
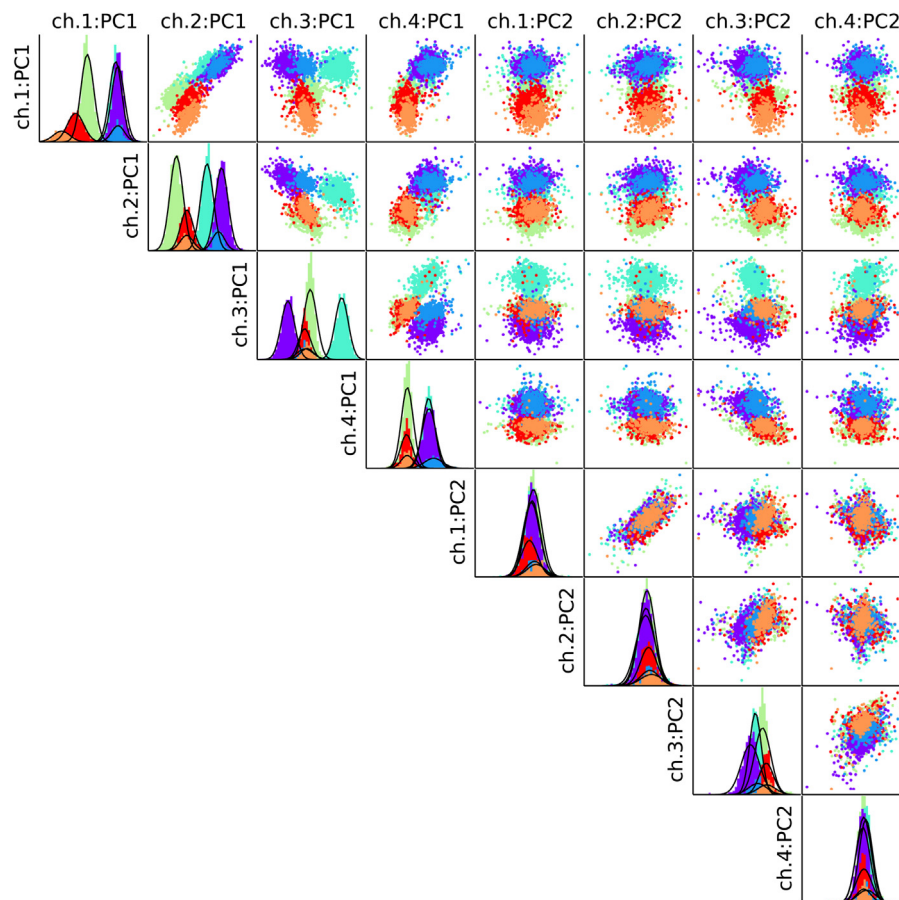
Fig. 10. Projections of principal components (PCs) of spike waveforms for example tetrode benchmarking data set. Projection of two first PCs of spike waveforms as recorded by the four tetrode channels. The colors depict different neurons, cf. Fig. 9. (For interpretation of the references to color in this figure legend, the reader is referred to the web version of the article.)

is shown in Fig. 11, the somatic membrane potentials of each neuron in panel a and corresponding, band-pass filtered extracellular potentials in panel b.

The resulting spike patterns of the 16 model neurons were found to cover a wide spectrum: some cells were quite bursty (see, e.g., cell 10 in Fig. 11a), some cells produced well separated firing events. (e.g., cell 16), while some neurons had quite small firing rates (cells 1 and 8 do not fire a single spike in the one-second excerpt considered in Fig. 11), see the figure for overview of firing rates.

In Fig. 12 we show the collection of spike-triggered waveforms across all 16 channels for 8 of the 16 model neurons. Typically the spikes can be observed on between three and six contacts. For some neurons, in particular, those positioned close to the polytrode shank, an inversion of the spike waveform can be clearly seen between two contacts, e.g., between contacts 5 and 6 for cell 13. At these contacts the spike amplitude is also seen to be largest (Somogyvári et al., 2005). Channels below the soma location displayed a negative initial peak (expectedly due to the dominance of fast inward Na^+ current in the soma in driving the extracellular potentials) while channels above displayed a positive initial peak (expectedly due to the dominance of reactive, capacitive membrane currents along the main apical dendrites of the neurons) (Pettersen and Einevoll, 2008; Pettersen et al., 2008).

3.4. Microelectrode array (MEA) benchmarking data

As the final example of benchmarking data sets we consider high-density microelectrode array (MEA) data mimicking recordings of spikes from salamander retina (Segev et al., 2004). Here

a total of 53 salamander retinal ganglion cells (Sheasby and Fohlmeister, 1999) were distributed across a virtual MEA chip spanning 102 recording electrodes as depicted in Fig. 13a. The large number of neurons and contacts employed here also serves to illustrate that the present simulation methodology is scalable to large systems. Despite of practical limitations in terms of system memory when increasing the number of electrode channels, we here successfully generated 1-min long benchmarking data sets including more than a hundred recording channels. Synthesized noise signals were produced based on *in vitro* mouse retinal recordings obtained with a Hierlemann MEA (Hierlemann et al., 2011; Frey et al., 2009, 2010; Fiscella et al., 2012) (as we did not have access to corresponding salamander recordings). However, for the present purposes of benchmarking data production, we judge this to be adequate. Further, the extracellular forward model was adapted by the method of images to incorporate the different extracellular conductivities of the retinal tissue, MEA chip, and saline bath (Ness et al., 2015); see Section 2.4.

An example of an averaged spike waveform for an example retinal ganglion cell across all included channels, is shown in Fig. 13b. As seen here, the spike can be clearly discerned at more than 10 of the closely spaced contacts (18 μm contact distance). Interestingly, the amplitude decay in the lateral direction was found to follow an approximately exponential fall-off with a fitted decay constant of $\lambda_d = 27.1$ μm (Fig. 13c), very close to previous experimental observations, i.e., $\lambda_d = 28 \pm 1$ μm (Segev et al., 2004). However, as the morphologies of the cell models in the population were different, their lateral amplitude-decay space constants showed some variability (not shown).
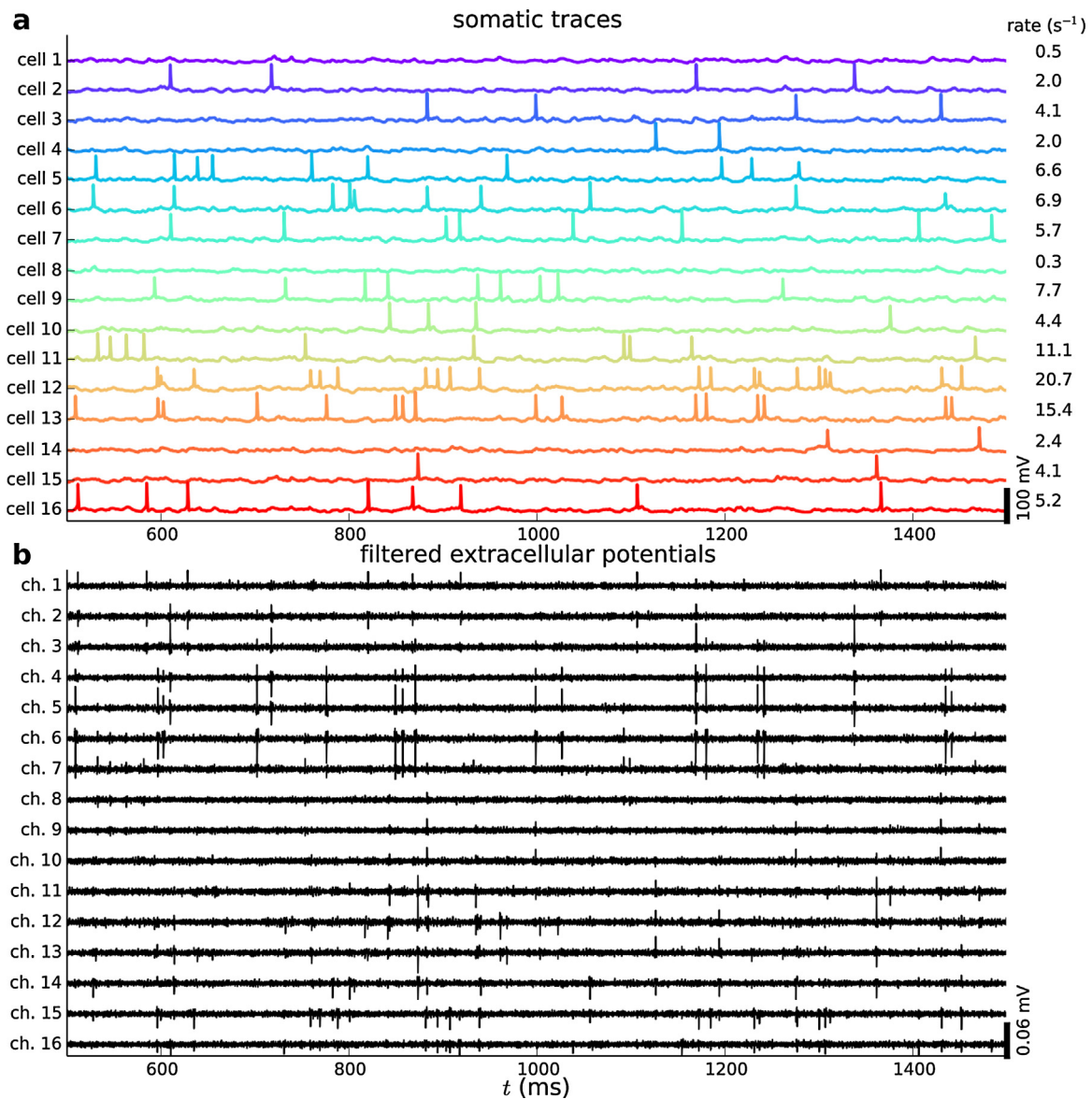
Fig. 11. Excerpts of intracellular and extracellular recordings for the 16 cells included in the example 16-channel polytrode benchmarking data set. (a) Somatic membrane potentials. Firing rates of cells 1–16 averaged over the 120 s real-time duration of the simulation are listed on the right hand side. (b) Superposition of extracellular potentials from all neurons and model noise, after band-pass filtering.

The retinal ganglion cells were activated by a simplified model of noisy synaptic input currents (cf. Section 2.4) resulting in spike trains with a substantial spread in interspike intervals (ISIs), cf. Fig. 13d. The excerpt of our example benchmarking data (Fig. 13e) showing both intracellular and extracellular signals corresponding to firing of an example cell, shows that its spikes are observed at several neighboring contacts.

4. Discussion

In this paper we have presented ViSAPy (Virtual Spiking Activity in Python), a general simulation tool for generating benchmarking data for evaluation of spike-sorting algorithms. The tool is based on a well-established biophysical forward-modeling scheme (Holt and Koch, 1999; Einevoll et al., 2013a) and is implemented as a Python package building on top of the neuronal simulator NEURON (Hines et al., 2009) and the Python tool LFPy for calculating extracellular potentials (Lindén et al., 2014), while NEST was used for simulating point-neuron networks

(Gewaltig and Diesmann, 2007) providing noisy synaptic input times to the test population. ViSAPy allows for arbitrary combinations of multicompartmental neuron models and geometries of recording electrodes and goes beyond presently available tools in several ways. For example, the tool allows for (i) addition of biologically realistic model noise extracted from experiments, (ii) activation of model neurons by controlled noisy synaptic inputs from recurrent spike networks generating in vivo like variation in spike shapes, (iii) inclusion of finite-sized disc-electrode contacts, and (iv) going beyond the common assumption of assuming infinite homogeneous volume conductors around the spiking model neurons allowing for generation of benchmarking data relevant for the in vitro microelectrode array (MEA) situation. Importantly, ViSAPy has been optimized to allow for generation of long time series of benchmarking data, spanning minutes of biological time, by parallel execution on multi-core computers.

We first investigated in detail how the recorded spike waveform depends on recording distance and size of electrode contacts.
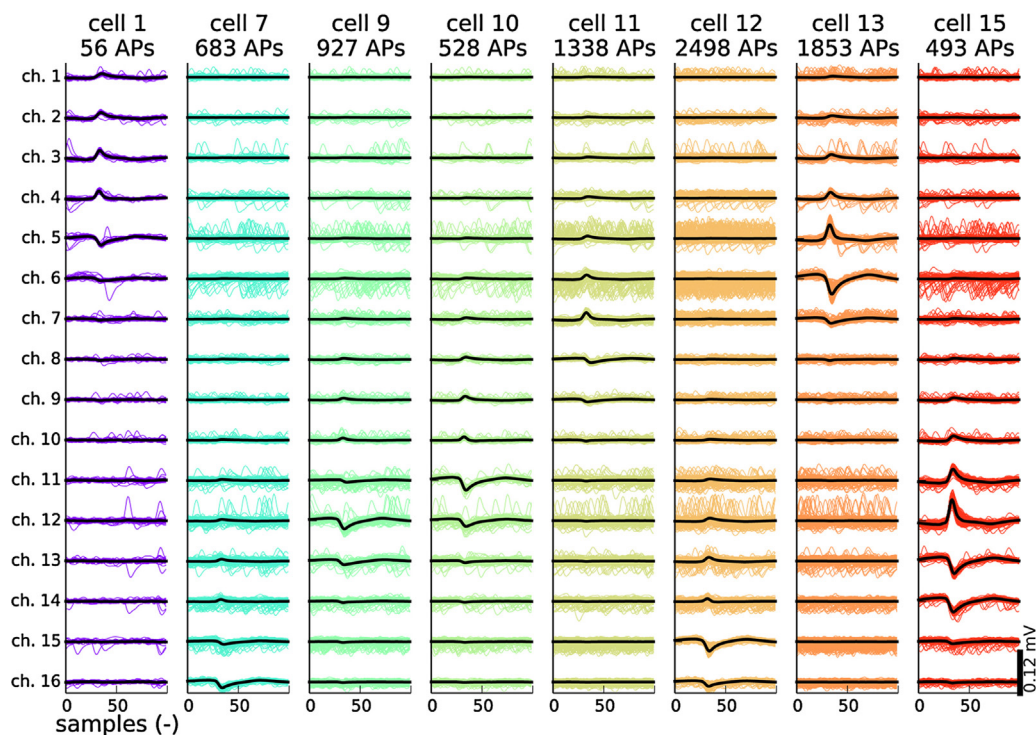
Fig. 12. Extracellular spike waveforms from polytrode benchmarking data set. Raw (colored lines) and spike-averaged (black lines) waveforms across 16 polytrode channels for eight (of 16) representative model neurons. The number below each cell designation corresponds to spike count during 120 s simulation period.

In agreement with previous findings we found that spike width increases with lateral distance x from the soma (Gold et al., 2006; Pettersen and Einevoll, 2008) and that for large x the spike amplitudes decayed with distance as $\sim x^{-2}$ (as for a current dipole), cf. Fig. 4 (Pettersen and Einevoll, 2008). We further found that for somas positioned very close to the electrode ($\lesssim 20 - 30\,\mu m$ for our layer 5b pyramidal neuron model (Hay et al., 2011)), a finite-sized disc electrode contact will both reduce the spike amplitude and increase the spike width, cf. Fig. 4. For larger distances, the effects of the physical extension of the electrodes were seen to be minor.

Experimental data, in particular *in vivo* recordings, are typically quite noisy, and benchmarking data must incorporate this in order to be a proper test bed for spike-sorting algorithms (Einevoll et al., 2012). Previously, this has been added in model-based benchmarking data by including noise generated by distant model neurons as well as thermal noise (Martinez et al., 2009; Lempka et al., 0450; Thorbergsson et al., 2002; Camuñas Mesa and Quiroga, 2013). Another alternative is to use experimentally recorded noise (Harris et al., 2000; Einevoll et al., 2012), and here we have implemented a new method for generating model noise extracted from experiments. As exemplified by the results in Fig. 7 for *in vivo* cortical noise, the generated model noise is very similar to the experimentally recorded noise, both in terms of frequency content and correlations across channels.

In order to increase the low-frequency variability of the spike firing in the ring network driving our multicompartmental model neurons, we added extra excitatory synaptic input to the network at spike times generated by non-stationary Poisson processes. These Poisson processes were in turn modulated by the synthetic model noise, cf. Appendix A. Without this extra input we observed that the spike rates lacked much of the frequency power at lower frequencies and irregularity that may occur in biological networks. While irregular noisy spike patterns also can be obtained in spatially unstructured networks (Brunel, 2000), we found that it was easier

to control the synaptic inputs onto the spike-generating multicompartmental model neurons (in particular the correlation structure) with the present structured network (Kriener et al., 2009). Note, however, that we here put no particular biological significance to the ring-network model and its non-stationary input itself, it was simply a practical tool for driving the multicompartmental neurons to give biologically plausible characteristics of firing rates and spike waveform variability.

We considered three example benchmarking data sets, i.e., tetrode and polytrode data mimicking *in vivo* cortical recordings and MEA recordings of *in vitro* activity in salamander retinas. In the generation of the cortical data we used biophysically detailed layer 5b pyramidal neuron models previously shown to exhibit both regular (tonic) and bursting spiking behavior (Hay et al., 2011). In combination with the present network-generated noisy synaptic input, the resulting benchmarking data were found to exhibit key features seen in experimental spike recordings, i.e., a large variability in spike waveforms and a large variation in neural firing rates. In particular the former feature represents a main challenge in the development of automatic spike-sorting methods (Einevoll et al., 2012). Specifically, the benchmarking data exhibited a clear dependence of the spike waveform on the time since the previous spike of the same neuron, i.e., the interspike interval (ISI): short ISIs, like follow-up spikes in bursts, had substantially smaller spike amplitudes than spikes preceded by long ISIs. This is in accordance with experimental findings (Fee et al., 1996; Quirk and Wilson, 1999; Henze et al., 2000; Buzsáki, 2004; Stratton et al., 2012).

The benchmarking data mimicking *in vitro* recordings from salamander retinas was tuned to be similar to the experimental MEA recordings in Segev et al. (2004). In fact, with the reconstructed salamander retinal ganglion cells placed about 15 μm above the MEA chip surface, essentially the same decay of the recorded spike amplitude with lateral distance was seen in our model benchmarking data (Fig. 13) as in the experiments (Segev et al., 2004).
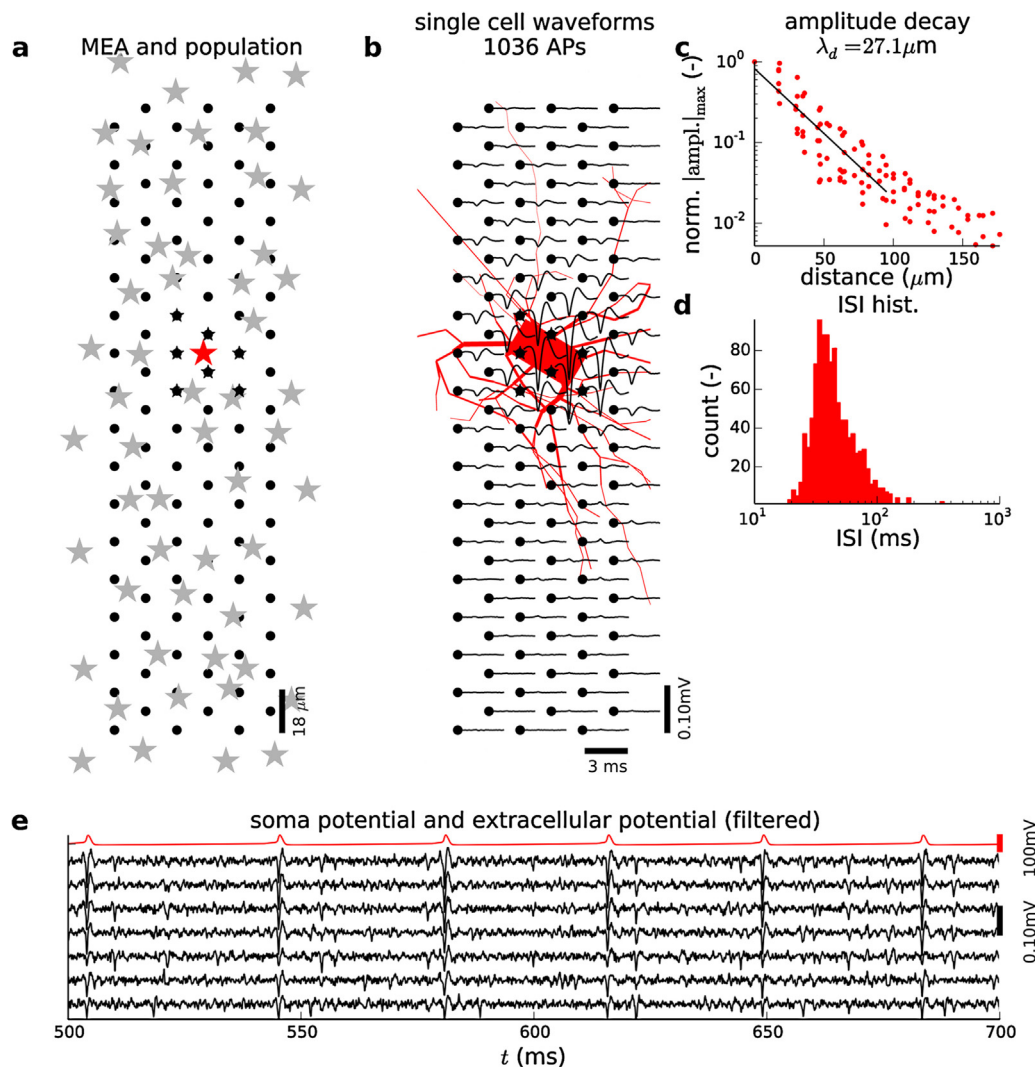
Fig. 13. Illustration of setup for generation of benchmarking data for *in vitro* retinal recording with high-density MEAs. (a) Electrode contacts (dots) and population of salamander retinal ganglion cells (stars). (b) Illustration of neuronal morphology (red) of retinal ganglion cell marked with red star in (a). The spike-averaged waveform of the same cell is also shown. (c) Dependence of spike amplitude from red example ganglion cell with lateral distance in the MEA plane. Black straight line represents best fit to exponentially decaying function (fitted using quasi-Newton Broyden–Fletcher–Goldfarb–Shanno (BFGS) method) with a spatial decay constant $\lambda_d = 27.1\,\mu$m. (d) Histogram of ISI distribution for the red example cell for a simulation lasting 60 s real time. (e) Soma membrane potential (red trace) and filtered extracellular potentials in the seven closest electrode channels (black traces) to the example cell, ordered from top to bottom according to distance between MEA contact and soma center (red star in (a)). (For interpretation of the references to color in this figure legend, the reader is referred to the web version of the article.)

While we here have produced benchmarking data sets for common *in vivo* and *in vitro* spike-recording situations, it should be emphasized that our approach for generating spike-sorting benchmarking data is open-ended. For example, spiking from an arbitrary combination of different model neurons, both excitatory and inhibitory, can be considered. Further, our electrode models can be extended to take into account other multielectrode geometries (Buzsáki, 2004), shadowing effects from the electrode shank (Mechler and Victor, 2011), or include more complicated geometries and inhomogeneous electrical conductivities in MEAs (Ness et al., 2015). The scheme can also easily be adapted to include spatial electrode drift (Franke et al., 2010).

To facilitate new applications, ViSAPy has been designed so that each main component, e.g., models for synaptic activation, extracellular noise, individual neurons and neural populations, are represented as Python class objects. The classes are part of a Python package released under GPLv3, and should run on most platforms, though preferably on high performance computing facilities. The code is available on GitHub (https://github.com/espenhgn/ViSAPy).

Our focus here has been on generating benchmarking data for testing of spike-sorting algorithms. However, ViSAPy can, of course, also be used to get direct explanatory insight into the link between neural activity and what is measured with extracellular electrodes (Holt and Koch, 1999; Gold et al., 2006; Pettersen et al., 2008, 2012; Pettersen and Einevoll, 2008; Lindén et al., 2010, 2011; Einevoll et al., 2013a,b; Łęski et al., 2013; Reimann et al., 2013). The present observation that the salamander retinal ganglion cells appears to be located about 15 μm above the MEA surface in the experiments of Segev et al. (2004), is an example of this. Note also that the biophysical forward-modeling scheme in ViSAPy is equally valid for calculating the low-frequency components of the extracellular potential, i.e., the local field potential (Einevoll et al., 2013a,b).

Presently, there are several large-scale neuroscience research initiatives such as the EU Human Brain Project (http://humanbrainproject.eu), the US BRAIN initiative (Insel et al., 2013; Devor et al., 2013) and Project MindScope at the Allen Brain Institute (https://www.alleninstitute.org/our-research/research-science/mindscope), on the way. One of the ambitions is to develop

new multielectrodes to record spikes from unprecedented large number of neurons, thousands or more. However, this potential can only be realized if advances in electrode hardware are followed up by development of validated automatic spike-sorting methods (Einevoll et al., 2012). This development has been severely hampered by lack of benchmarking data sets with known ground truth against which the various spike-sorting algorithms can be tested.

Validation of spike-sorting methods will require two main components: (i) a suite of benchmarking data where the ground truth is known (whether modeled as here or obtained directly from experiments (Harris et al., 2000)) and (ii) a virtual meeting place where benchmarking data can meet spike-sorting algorithms (Denker et al., 2014). A first prototype of such a virtual meeting place is presently available at the German national node of International Neuroinformatics Coordinating Facility (INCF, http://spike.g-node.org). It is indeed our belief and hope that much needed reliable, efficient and accurate automatic spike-sorting algorithms can be developed by a community effort.

Appendix A. Spiking neuron network model for *in vivo* like synaptic activation

For the benchmarking data emulating *in vivo* recordings, we used a structured spiking neuron network with a 1D ring topology adapted from Kriener et al. (2009) in order to generate synapse activation times. The network comprised 12 500 leaky integrate-and-fire (LIF) neurons, with $N_E = 10\,000$ excitatory neurons and $N_I = 2500$ inhibitory neurons, connected such that every fifth neuron on the ring was inhibitory. Each neuron was connected to its κ nearest neighbors with current-based synapses (δ-currents). For a full network description, see Kriener et al. (2009). The parameters are summarized in Table 3. The network simulations were implemented in NEST (Gewaltig and Diesmann, 2007) using PyNEST (Eppler et al., 2008).

In addition to the recurrent interactions in the network, each of the ring-network neurons received additional spiking input generated by non-stationary Poisson processes (Brown et al., 2002), $S(t)$, with mean rate expectation of $\upsilon_{\text{ext.noise}}$. The rate function of the Poisson process for the excitatory population, $\lambda_E(t)$, was calculated from the synthesized noise traces (cf. Section 2.6), that we *a priori* averaged over the spatial dimension (i.e., across electrode contacts), band-pass filtered (using a 2nd order Butterworth bandpass filter with cutoff frequencies of 1 and 25 Hz), normalized between zero and one, inverted, and multiplied with

$2\upsilon_{\text{ext.noise}}$. For the inhibitory cells, $\lambda_I(t) = 2\upsilon_{\text{ext.noise}} - \lambda_E(t)$. The procedure effectively increased network-population firing rates during downward deflections of extracellular noise, and the overall excitatory synaptic input to the multicompartment target neurons.

The network simulation was run for the entire duration of the corresponding benchmarking data, and all spike events in the excitatory and inhibitory populations were recorded and stored in `sqlite3` databases, i.e., so that we could efficiently request spike trains of individual neurons later. In order to connect spike trains occurring in some part of the network to each n out of the the N post-synaptic, multicompartmental model neurons, we drew for each cell's total number of synapses ($n_{\text{syn,E}} + n_{\text{syn,I}}$) random samples from a von Mises distribution (Mardia and Jupp, 2009). The probability density function for an angle θ was here then defined as

$$f(\theta | \mu_n, \kappa_n) = \frac{\exp(\kappa_n \cos(\theta - \mu_n))}{2\pi I_0(\kappa_n)}. \tag{A.1}$$

Here, κ_n is the reciprocal dispersion, μ_n the center of the distribution corresponding to cell n, and I_0 the 0th order modified Bessel function.

The uniformly distributed random angles on the interval $[0, 2\pi)$ radians for each postsynaptic cell n, were scaled to span the upper and lower range of cell indices of inhibitory and excitatory populations in the network before rounding off to the nearest integer value. Assuming an angular neuron density of $5000/\pi$ rad^{-1} and $1250/\pi$ rad^{-1}, respectively, for the excitatory and inhibitory populations, that we multiplied with the random angles and rounded off to the nearest integer values, output values served as indices allowing us to pick synapse activation times for each synapse on a postsynaptic cell from a spatially confined part of the ring network topology. The parameters for the generation of non-stationary Poisson spiketrains and the mapping of spike trains to synapses are summarized in Table 3 for each set of generated benchmark data.

Appendix B. Method of images

Given a single current point source I at position (x', y', z') in a three-layered medium, i.e., a lower, non-conducting glass electrode plate, an electrically homogeneous brain tissue slice centered in the xy-plane and with vertical extension from $z = 0$ to $z = h$, and an infinitely thick saline layer covering the brain slice, the extracellular potential at the electrode-slice boundary ($z = 0$) is given by Ness et al. (2015) and Barrera et al. (1978) as

$$\Phi_{\text{PS}}(x, y, 0) = 2\Phi_h(x - x', y - y', -z') + 2\sum_{n=1}^{\infty} \left(\frac{\sigma_T - \sigma_S}{\sigma_T + \sigma_S}\right)^n$$
$$\times \left(\Phi_h(x - x', y - y', -z' + 2nh) \right.$$
$$\left. + \Phi_h(x - x', y - y', -z' - 2nh)\right), \tag{B.1}$$

where

$$\Phi_h(u, v, w) \equiv \frac{I}{4\pi\sigma_T(u^2 + v^2 + w^2)^{1/2}}$$

is the potential generated around a current point source I positioned at $u = v = w = 0$ in an infinite, homogenous electrical conductor with the conductivity of the brain tissue σ_T. Further, σ_T is the conductivity of the saline. The sum over N should in principle go to infinity, but the series converges fast, and $N = 20$ is for practical applications both sufficiently accurate and fast to compute (Ness et al., 2015).

Eq. (B.1) assumes that the transmembrane currents from each compartment can be treated as point sources. The corresponding

line source equation (Holt and Koch, 1999), for a compartment extending from (x'_0, y'_0, z'_0) to (x'_1, y'_1, z'_1), takes the form:

$$\Phi_{LS}(x, y, 0) = 2\tilde{\Phi}_h(x - x'_0, y - y'_0, -z'_0) + 2\sum_{n=1}^{\infty}\left(\frac{\sigma_T - \sigma_S}{\sigma_T + \sigma_S}\right)^n$$
$$\times\left(\tilde{\Phi}_h(x - x'_0, y - y'_0, -z'_0 + 2nh)\right.$$
$$\left. + \tilde{\Phi}_h(x - x'_0, y - y'_0, -z'_0 - 2nh)\right), \quad (B.2)$$

where the auxiliary potential variable $\tilde{\Phi}_h$ is introduced as

$$\tilde{\Phi}_h(u, v, w) \equiv \frac{I}{4\pi\sigma_T \Delta s}$$
$$\times \ln\left(\frac{\Delta s^2 - \gamma(u, v, w) + \Delta s\sqrt{\Delta s^2 - 2\gamma(u, v, w) + \rho(u, v, w)^2}}{-\gamma(u, v, w) + \rho(u, v, w)\Delta s}\right), \quad (B.3)$$

where

$$\gamma(u, v, w) \equiv u(x'_1 - x'_0) + v(y'_1 - y'_0) + w(z'_1 - z'_0), \quad (B.4)$$

$$\rho(u, v, w) \equiv (u^2 + v^2 + w^2)^{1/2}, \quad (B.5)$$

and

$$\Delta s \equiv ((x'_1 - x'_0)^2 + (y'_1 - y'_0)^2 + (z'_1 - z'_0)^2)^{1/2} \quad (B.6)$$

is the length of the axis of the cylindrical compartment.

Again, we summed over 20 terms ($N = 20$), although Eq. (B.1) and (B.2) involves a sum over an infinite series.

Appendix C. `ViSAPy` **Python package**

All simulation codes have been made available on GitHub, https://github.com/espenhgn/ViSAPy. For information on installation and usage, refer to the provided documentation and example files.

Generated benchmark data are stored using platform-independent HDF5 format (The HDF Group, 2000–2010) for further distribution. The main output files contain two datasets: `data` is an $n_{timesteps}$ times $n_{channels}$ array of floats with the electric potentials in units of mV, the sampling rate `srate` is an integer or float value in Hz. The file containing the ground-truth spiking times is pure text, containing two space-separated columns of integers, the first column is cell index, the second column the spike time index (cf. Section 2.7).

References

Arthur D, Vassilvitskii S. K-means++: the advantages of careful seeding. In: Proceedings of the 18th annual ACM-SIAM symposium on discrete algorithms. SODA'07. Philadelphia, PA, USA: Society for Industrial and Applied Mathematics; 2007. p. 1027–35, URL http://dl.acm.org/citation.cfm?id=1283383.1283494

Bahl A, Stemmler MB, Herz AVM, Roth A. Automated optimization of a reduced layer 5 pyramidal cell model based on experimental data. J Neurosci Methods 2012;210(September (1)):22–34, http://dx.doi.org/10.1016/j.jneumeth.2012.04.006.

Barrera RG, Guzmán O, Balaguer B. Point charge in a three-layered dielectric medium with planar interfaces. Am J Phys 1978;46(11):1172–9, http://dx.doi.org/10.1119/1.11501.

Blanche TJ, Spacek MA, Hetke JF, Swindale NV. Polytrodes: high-density silicon electrode arrays for large-scale multiunit recording. J Neurophysiol 2005;93(May (5)):2987–3000, http://dx.doi.org/10.1152/jn.01023.2004.

Brainard DH. The psychophysics toolbox. Spat Vis 1997;10(4):433–6, http://dx.doi.org/10.1163/156856897X00357.

Brown EN, Barbieri R, Ventura V, Kass RE, Frank LM. The time-rescaling theorem and its application to neural spike train data analysis. Neural Comput 2002;14(February (2)):325–46, http://dx.doi.org/10.1162/08997660252741149.

Brunel N. Dynamics of sparsely connected networks of excitatory and inhibitory spiking neurons. J Comput Neurosci 2000;8(3):183–208, URL http://www.ncbi.nlm.nih.gov/pubmed/10809012

Buzsáki G. Large-scale recording of neuronal ensembles. Nat Neurosci 2004;7(May (5)):446–51, http://dx.doi.org/10.1038/nn1233.

Camuñas Mesa LA, Quiroga RQ. A detailed and fast model of extra-cellular recordings. Neural Comput 2013;25(March (5)):1191–212, http://dx.doi.org/10.1162/NECO_a_00433.

Deb K, Kalyanmoy D. Multi-objective optimization using evolutionary algorithms. New York, NY, USA: John Wiley & Sons, Inc; 2001.

Delescluse M, Pouzat C. Efficient spike-sorting of multi-state neurons using inter-spike intervals information. J Neurosci Methods 2006;150(January (1)):16–29, http://dx.doi.org/10.1016/j.jneumeth.2005.05.023.

Denker M, Einevoll GT, Franke F, Grün S, Hagen E, Kerr J, et al. Report from 1st INCF workshop on validation of analysis methods, Tech. rep. International Neuroinformatics Coordinating Facility (INCF); 2014.

Destexhe A, Paré D. Impact of network activity on the integrative properties of neo-cortical pyramidal neurons in vivo. J Neurophysiol 1999;81(April (4)):1531–47, URL http://jn.physiology.org/content/81/4/1531

Destexhe A, Rudolph M, Fellous J-M, Sejnowski T. Fluctuating synaptic conductances recreate in vivo-like activity in neocortical neurons. Neuroscience 2001;107(1):13–24, http://dx.doi.org/10.1016/S0306-4522(01)00344-X.

Devor A, Bandettini PA, Boas DA, Bower JM, Buxton RB, Cohen LB, et al. The challenge of connecting the dots in the B.R.A.I.N. Neuron 2013;80(October (2)):270–4, http://dx.doi.org/10.1016/j.neuron.2013.09.008.

Druckmann S, Banitt Y, Gidon A, Schürmann F, Markram H, Segev I. A novel multiple objective optimization framework for constraining conductance-based neuron models by experimental data. Front Neurosci 2007;1(November (1)):7–18, http://dx.doi.org/10.3389/neuro.01.1.1.001.2007.

Eaton KP, Henriquez CS. Confounded spikes generated by synchrony within neural tissue models. Neurocomputing 2005;65–66:851–7, http://dx.doi.org/10.1016/j.neucom.2004.10.082.

Einevoll G, Kayser C, Logothetis N, Panzeri S. Modelling and analysis of local field potentials for studying the function of cortical circuits. Nat Rev Neurosci 2013a;14:770–85, http://dx.doi.org/10.1038/nrn3599.

Einevoll GT, Franke F, Hagen E, Pouzat C, Harris KD. Towards reliable spike-train recordings from thousands of neurons with multielectrodes. Curr Opin Neurobiol 2012;22(February (1)):11–7, http://dx.doi.org/10.1016/j.conb.2011.10.001.

Einevoll GT, Lindén H, Tetzlaff T, Łęski S, Pettersen KH. Local field potential: biophysical origin and analysis. In: Quiroga RQ, Panzeri S, editors. Principles of neural coding. CRC Press; 2013b.

Eppler JM, Helias M, Müller E, Diesmann M, Gewaltig M-O. PyNEST: a convenient interface to the NEST simulator. Front Neuroinform 2008;2(January):12, http://dx.doi.org/10.3389/neuro.11.012.2008.

Fee MS, Mitra PP, Kleinfeld D. Automatic sorting of multiple unit neuronal signals in the presence of anisotropic and non-Gaussian variability. J Neurosci Methods 1996;69(November (2)):175–88, http://dx.doi.org/10.1016/S0165-0270(96)00050-7.

Fee MS, Mitra PP, Kleinfeld D. Variability of extracellular spike waveforms of cortical neurons. J Neurophysiol 1996;76(December (6)):3823–33, URL http://jn.physiology.org/content/76/6/3823

Field DJ. Relations between the statistics of natural images and the response properties of cortical cells. J Opt Soc Am A 1987;4(December (12)):2379–94, http://dx.doi.org/10.1364/JOSAA.4.002379.

Fiscella M, Farrow K, Jones IL, Jäckel D, Müller J, Frey U, et al. Recording from defined populations of retinal ganglion cells using a high-density CMOS-integrated microelectrode array with real-time switchable electrode selection. J Neurosci Methods 2012;211(October (1)):103–13, http://dx.doi.org/10.1016/j.jneumeth.2012.08.017.

Franke F, Jäckel D, Dragas J, Müller J, Radivojevic M, Bakkum D, et al. High-density microelectrode array recordings and real-time spike sorting for closed-loop experiments: an emerging technology to study neural plasticity. Front Neural Circuits 2012;6:105, http://dx.doi.org/10.3389/fncir.2012.00105.

Franke F, Natora M, Meier P, Hagen E, Pettersen KH, Linden H, et al. An automated online positioning system and simulation environment for multi-electrodes in extracellular recordings. Conf Proc IEEE Eng Med Biol Soc 2010;2010:593–7, http://dx.doi.org/10.1109/IEMBS.2010.5626631.

Frey U, Egert U, Heer F, Hafizovic S, Hierlemann A. Microelectronic system for high-resolution mapping of extracellular electric fields applied to brain slices. Biosens Bioelectron 2009;24(March (7)):2191–8, http://dx.doi.org/10.1016/j.bios.2008.11.028.

Frey U, Sedivy J, Heer F, Pedron R, Ballini M, Mueller J, et al. Switch-matrix-based high-density microelectrode array in cmos technology. IEEE J Solid-State Circuits 2010;45(February (2)):467–82, http://dx.doi.org/10.1109/JSSC.2009.2035196.

Gewaltig M-O, Diesmann M. Nest (neural simulation tool). Scholarpedia 2007;2(4):1430, URL http://www.scholarpedia.org/article/NEST_(NEural_Simulation_Tool)

Gold C, Girardin CC, Martin KAC, Koch C. High-amplitude positive spikes recorded extracellularly in cat visual cortex. J Neurophysiol 2009;102(December (6)):3340–51, http://dx.doi.org/10.1152/jn.91365.2008.

Gold C, Henze DA, Koch C. Using extracellular action potential recordings to constrain compartmental models. J Comput Neurosci 2007;23(August (1)):39–58, http://dx.doi.org/10.1007/s10827-006-0018-2.

Gold C, Henze DA, Koch C, Buzsáki G. On the origin of the extracellular action potential waveform: a modeling study. J Neurophysiol 2006;95(May (5)):3113–28, http://dx.doi.org/10.1152/jn.00979.2005.

Goto T, Hatanaka R, Ogawa T, Sumiyoshi A, Riera J, Kawashima R. An evaluation of the conductivity profile in the somatosensory barrel cortex of Wistar rats. J Neurophysiol 2010;104(December (6)):3388–412, http://dx.doi.org/10.1152/jn.00122.2010.

Gray CM, Maldonado PE, Wilson M, McNaughton B. Tetrodes markedly improve the reliability and yield of multiple single-unit isolation from multi-unit recordings in cat striate cortex. J Neurosci Methods 1995;63(December (1–2)):43–54, URL http://www.ncbi.nlm.nih.gov/pubmed/8788047

Hämäläinen M, Haari R, Ilmoniemi RJ, Knuutila J, Lounasmaa OV. Magnetoencephalography – theory, instrumentation, and application to noninvasive studies of the working human brain. Rev Mod Phys 1993;65:413–96, http://dx.doi.org/10.1103/RevModPhys.65.413.

Harris KD, Henze DA, Csicsvari J, Hirase H, Buzsáki G. Accuracy of tetrode spike separation as determined by simultaneous intracellular and extracellular measurements. J Neurophysiol 2000;84(July (1)):401–14, URL http://jn.physiology.org/content/84/1/401

Harris KD, Hirase H, Leinekugel X, Henze DA, Buzsáki G. Temporal interaction between single spikes and complex spike bursts in hippocampal pyramidal cells. Neuron 2001;32(October (1)):141–9, http://dx.doi.org/10.1016/S0896-6273(01)00447-0.

Hay E, Hill S, Schürmann F, Markram H, Segev I. Models of neocortical layer 5b pyramidal cells capturing a wide range of dendritic and perisomatic active properties. PLoS Comput Biol 2011;7(July (7)):e1002107, http://dx.doi.org/10.1371/journal.pcbi.1002107.

Hay E, Schürmann F, Markram H, Segev I. Preserving axosomatic spiking features despite diverse dendritic morphology. J Neurophysiol 2013;109(June (12)):2972–81, http://dx.doi.org/10.1152/jn.00048.2013.

Hendrickson EB, Edgerton JR, Jaeger D. The capabilities and limitations of conductance-based compartmental neuron models with reduced branched or unbranched morphologies and active dendrites. J Comput Neurosci 2011;30(April (2)):301–21, http://dx.doi.org/10.1007/s10827-010-0258-z.

Henze DA, Borhegyi Z, Csicsvari J, Mamiya A, Harris KD, Buzsáki G. Intracellular features predicted by extracellular recordings in the hippocampus in vivo. J Neurophysiol 2000;84(July (1)):390–400, URL http://jn.physiology.org/content/84/1/390

Hierlemann A, Frey U, Hafizovic S, Heer F. Growing cells atop microelectronic chips: interfacing electrogenic cells in vitro with cmos-based microelectrode arrays. Proc IEEE 2011;99(February (2)):252–84, http://dx.doi.org/10.1109/JPROC.2010.2066532.

Hill DN, Mehta SB, Kleinfeld D. Quality metrics to accompany spike sorting of extracellular signals. J Neurosci 2011;31(June (24)):8699–705, http://dx.doi.org/10.1523/JNEUROSCI.0971-11.2011.

Hines ML, Davison AP, Müller E. Neuron and python. Front Neuroinform 2009;3:1–12, http://dx.doi.org/10.3389/neuro.11.001.2009.

Hines ML, Morse T, Migliore M, Carnevale NT, Shepherd GM. ModelDB: a database to support computational neuroscience. J Comput Neurosci 2004;17(1):7–11, http://dx.doi.org/10.1023/B:JCNS.0000023869.22017.2e.

Hockney RW. The science of computer benchmarking. United States: Society for Industrial & Applied Mathematics; 1996, http://dx.doi.org/10.1137/1.9780898719666.

Holt GR, Koch C. Electrical interactions via the extracellular potential near cell bodies. J Comput Neurosci 1999;6(March (2)):169–84, http://dx.doi.org/10.1023/A:1008832702585.

Insel TR, Landis SC, Collins FS. Research priorities. The NIH brain initiative. Science 2013;340(May (6133)):687–8, http://dx.doi.org/10.1126/science.1239276.

Kriener B, Helias M, Aertsen A, Rotter S. Correlations in spiking neuronal networks with distance dependent connections. J Comput Neurosci 2009;27(October (2)):177–200, http://dx.doi.org/10.1007/s10827-008-0135-1.

Kriener B, Helias M, Rotter S, Diesmann M, Einevoll GT. How pattern formation in ring networks of excitatory and inhibitory spiking neurons depends on the input current regime. Front Comput Neurosci 2014;7(187)., http://dx.doi.org/10.3389/fncom.2013.00187.

Lambacher A, Vitzthum V, Zeitler R, Eickenscheidt M, Eversmann B, Thewes R, et al. Identifying firing mammalian neurons in networks with high-resolution multi-transistor array (MTA). Appl Phys A 2011;102(1):1–11, http://dx.doi.org/10.1007/s00339-010-6046-9.

Langtangen H. A primer on scientific programming with Python. Mathematics and statistics. Berlin Heidelberg: Springer-Verlag; 2009, URL http://books.google.no/books?id=cVof07z_rA4C

Larson MG, Bengzon F. The finite element method: theory, implementation, and applications. Springer; 2013.

Łęski S, Lindén H, Tetzlaff T, Pettersen KH, Einevoll GT. Frequency dependence of signal power and spatial reach of the local field potential. PLoS Comput Biol 2013;9:e1003137, http://dx.doi.org/10.1371/journal.pcbi.1003137.

Le Bé J-V, Silberberg G, Wang Y, Markram H. Morphological, electrophysiological, and synaptic properties of corticocallosal pyramidal cells in the neonatal rat neocortex. Cereb Cortex 2007;17(September (9)):2204–13, http://dx.doi.org/10.1093/cercor/bhl127.

Lempka SF, Johnson MD, Moffitt MA, Otto KJ, Kipke DR, McIntyre CC. Theoretical analysis of intracortical microelectrode recordings. J Neural Eng 2011;8(August (4)):045006, http://dx.doi.org/10.1088/1741-2560/8/4/045006.

Lewicki MS. A review of methods for spike sorting: the detection and classification of neural action potentials. Network 1998;9(November (4)):R53–78, URL http://www.ncbi.nlm.nih.gov/pubmed/10221571

Lindén H, Hagen E, Łęski S, Norheim ES, Pettersen KH, Einevoll GT. LFPy: a tool for biophysical simulation of extracellular potentials generated by detailed model neurons. Front Neuroinform 2014;7(41)., http://dx.doi.org/10.3389/fninf.2013.00041.

Lindén H, Pettersen KH, Einevoll GT. Intrinsic dendritic filtering gives low-pass power spectra of local field potentials. J Comput Neurosci 2010;29(December (3)):423–44, http://dx.doi.org/10.1007/s10827-010-0245-4.

Lindén H, Tetzlaff T, Potjans T, Pettersen K, Grün S, Diesmann M, et al. Modeling the spatial reach of the LFP. Neuron 2011;72(December (5)):859–72, http://dx.doi.org/10.1016/j.neuron.2011.11.006.

Logothetis NK, Kayser C, Oeltermann A. In vivo measurement of cortical impedance spectrum in monkeys: implications for signal propagation. Neuron 2007;55(September (5)):809–23, http://dx.doi.org/10.1016/j.neuron.2007.07.027.

Mardia K, Jupp P. Directional statistics. Wiley series in probability and statistics. Wiley; 2009, http://dx.doi.org/10.1002/9780470316979.

Martinez J, Pedreira C, Ison MJ, Quiroga RQ. Realistic simulation of extracellular recordings. J Neurosci Methods 2009;184(November (2)):285–93, http://dx.doi.org/10.1016/j.jneumeth.2009.08.017.

Mechler F, Victor JD. Dipole characterization of single neurons from their extracellular action potentials. J Comput Neurosci 2011;32(1):73–100, http://dx.doi.org/10.1007/s10827-011-0341-0.

Menne KM, Folkers A, Malina T, Maex R, Hofmann UG. Test of spike-sorting algorithms on the basis of simulated network data. Neurocomputing 2002;44–46:1119–26, http://dx.doi.org/10.1016/S0925-2312(02)00432-0.

Nelson MJ, Pouget P. Do electrode properties create a problem in interpreting local field potential recordings? J Neurophysiol 2010;103(May (5)):2315–7, http://dx.doi.org/10.1152/jn.00157.2010.

Nelson MJ, Pouget P, Nilsen EA, Patten CD, Schall JD. Review of signal distortion through metal microelectrode recording circuits and filters. J Neurosci Methods 2008;169(March (1)):141–57, http://dx.doi.org/10.1016/j.jneumeth.2007.12.010.

Ness TB, Hagen E, Negwer M, Bakker R, Schubert D, Einevoll GT. Modeling extracellular spikes and local field potentials recorded in MEAs. In: Proceedings of the 8th international meeting on multielectrode arrays. Reutlingen, Germany: Natural and Medical Sciences Institute (NMI), University of Tübingen; 2012. p. 234–6, URL http://www.nmi1.de/meameeting2012/

Ness TV, Chintaluri C, Potworowski J, Łęski S, Głąbska H, Wójcik DK, et al. Modelling and analysis of electrical potentials recorded in microelectrode arrays (MEAs). Neuroinformatics 2015., http://dx.doi.org/10.1007/s12021-015-9265-6 [in press].

Nunez PL, Srinivasan R. Electric fields of the brain: the neurophysics of EEG. 2nd ed. Oxford University Press, Inc.; 2006, http://dx.doi.org/10.1093/acprof:oso/9780195050387.001.0001.

Palmer SE. Vision science: photons to phenomenology. Cambridge, MA: MIT Press; 1999, URL http://mitpress.mit.edu/books/vision-science

Pettersen KH, Einevoll GT. Amplitude variability and extracellular low-pass filtering of neuronal spikes. Biophys J 2008;94(February (3)):784–802, http://dx.doi.org/10.1529/biophysj.107.111179.

Pettersen KH, Hagen E, Einevoll GT. Estimation of population firing rates and current source densities from laminar electrode recordings. J Comput Neurosci 2008;24(June (3)):291–313, http://dx.doi.org/10.1007/s10827-007-0056-4.

Pettersen KH, Lindén H, Dale AM, Einevoll GT. Extracellular spikes and CSD. In: Brette R, Destexhe A, editors. Handbook of neural activity measurement. Cambridge University Press; September 2012. p. 92–135.

Pettersen KH, Lindén H, Tetzlaff T, Einevoll GT. Power laws from linear neuronal cable theory: power spectral densities of the soma potential, soma membrane current and single-neuron contribution to the eeg. PLoS Comput Biol 2014;10(11):e1003928, http://dx.doi.org/10.1371/journal.pcbi.1003928.

Pillow JW, Shlens J, Paninski L, Sher A, Litke AM, Chichilnisky EJ, et al. Spatio-temporal correlations and visual signalling in a complete neuronal population. Nature 2008;454(August (7207)):995–9, http://dx.doi.org/10.1038/nature07140.

Quirk MC, Wilson MA. Interaction between spike waveform classification and temporal sequence detection. J Neurosci Methods 1999;94(December (1)):41–52, http://dx.doi.org/10.1016/S0165-0270(99)00124-7.

Quiroga RQ. Spike sorting. Scholarpedia 2007;2(12):3583, URL http://www.scholarpedia.org/article/Spike_sorting

Rall W. Electrophysiology of a dendritic neuron model. Biophys J 1962;2(March (2 Pt 2)):145–67.

Ranck J Jr. Studies on single neurons in dorsal hippocampal formation and septum in unrestrained rats. I. Behavioral correlates and firing repertoires. Exp Neurol 1973;41(November (2)):461–531, URL http://www.ncbi.nlm.nih.gov/pubmed/4355646

Reimann MW, Anastassiou CA, Perin R, Hill SL, Markram H, Koch C. A biophysically detailed model of neocortical local field potentials predicts the

critical role of active membrane currents. Neuron 2013;79(July (2)):375–90, http://dx.doi.org/10.1016/j.neuron.2013.05.023.

Rinberg D, Davidowitz H, Tishby N. Multi-electrode spike sorting by clustering transfer functions. In: Kearns MS, Solla SA, Cohn D, editors. Advances in neural information processing systems, vol. 11. MIT Press; 1999.

Robinson D. The electrical properties of metal microelectrodes. Proc IEEE 1968;56(6):1065–71, http://dx.doi.org/10.1109/PROC.1968.6458.

Roth A, van Rossum CW. Modelling synapses. In: De Schutter E, editor. Computational modeling methods for neuroscientists. 1st ed. Cambridge, MA: MIT Press; 2009. p. 139–61 [Chapter 6], URL http://mitpress.mit.edu/books/computational-modeling-methods-neuroscientists

Segev R, Goodhouse J, Puchalla J, Berry MJ. Recording spikes from a large fraction of the ganglion cells in a retinal patch. Nat Neurosci 2004;7(October (10)):1154–61, http://dx.doi.org/10.1038/nn1323.

Segev R, Puchalla J, Berry MJ. Functional organization of ganglion cells in the salamander retina. J Neurophysiol 2006;95(April (4)):2277–92, http://dx.doi.org/10.1152/jn.00928.2005.

Sheasby BW, Fohlmeister JF. Impulse encoding across the dendritic morphologies of retinal ganglion cells. J Neurophysiol 1999;81(April (4)):1685–98, URL http://www.ncbi.nlm.nih.gov/pubmed/10200204

Smith LS, Mtetwa N. A tool for synthesizing spike trains with realistic interference. J Neurosci Methods 2007;159:170–80, http://dx.doi.org/10.1016/j.jneumeth.2006.06.019.

Somogyvári Z, Zalányi L, Ulbert I, Erdi P. Model-based source localization of extracellular action potentials. J Neurosci Methods 2005;147(September (2)):126–37, http://dx.doi.org/10.1016/j.jneumeth.2005.04.002.

Stratton P, Cheung A, Wiles J, Kiyatkin E, Sah P, Windels F. Action potential waveform variability limits multi-unit separation in freely behaving rats. PLoS ONE 2012;7(6):e38482, http://dx.doi.org/10.1371/journal.pone.0038482.

Taketani M, Baudry M, editors. Advances in network electrophysiology: using multielectrode arrays. Berlin: Springer; 2006.

Tetzlaff T, Diesmann M. Dependence of spike-count correlations on spike-train statistics and observation time scale. In: Grün S, Rotter S, editors. Analysis of parallel spike trains. Springer; 2010. p. 103–28, http://dx.doi.org/10.1007/978-1-4419-5675-0_6 [Chapter 6].

The HDF Group. Hierarchical data format version 5; 2000–2010, URL http://www.hdfgroup.org/HDF5

Thorbergsson P, Garwicz M, Schouenborg J, Johansson A. Statistical modelling of spike libraries for simulation of extracellular recordings in the cerebellum. In: Proc. 32nd annual international conference of the IEEE engineering in medicine and biology society (EMBS); 2010. p. 4250–3.

Thorbergsson PT, Garwicz M, Schouenborg J, Johansson AJ. Computationally efficient simulation of extracellular recordings with multielectrode arrays. J Neurosci Methods 2012;211(August (1)):133–44, http://dx.doi.org/10.1016/j.jneumeth.2012.08.011.

Tuckwell HC, Wan FYM, Rospars J-P. A spatial stochastic neuronal model with Ornstein–Uhlenbeck input current. Biol Cybern 2002;86(February (2)):137–45, http://dx.doi.org/10.1007/s004220100283.

Uhlenbeck GE, Ornstein LS. On the theory of the brownian motion. Phys Rev 1930;36(September):823–41, http://dx.doi.org/10.1103/PhysRev.36.823.

Ulbert I, Halgren E, Heit G, Karmos G. Multiple microelectrode-recording system for human intracortical applications. J Neurosci Methods 2001;106:69–79.

Van Geit W, De Schutter E, Achard P. Automated neuron model optimization techniques: a review. Biol Cybern 2008;99(November (4–5)):241–51, http://dx.doi.org/10.1007/s00422-008-0257-6.

Wood F, Black MJ, Vargas-Irwin C, Fellows M, Donoghue JP. On the variability of manual spike sorting. IEEE Trans Biomed Eng 2004;51(June (6)):912–8., http://dx.doi.org/10.1109/TBME.2004.826677.